APPLYING ULTRASOUND ELASTOGRAPHY TO DETECTING SKELETAL MUSCLE INJURY

A Dissertation

Presented to the Faculty of the Graduate School

of Cornell University

In Partial Fulfillment of the Requirements for the Degree of

Doctor of Philosophy

by

Matthew Joseph Leineweber

August 2014

APPLYING ULTRASOUND ELASTOGRAPHY TO

DETECTING SKELETAL MUSCLE INJURY

Matthew Joseph Leineweber, Ph. D.

Cornell University 2014

Skeletal muscle injuries are frequent in sports and exercise, accounting for between 20-55% of all sports injuries, with the vast majority of these injuries being muscle strains or contusions. Although muscle injuries are primarily diagnosed through symptomatology and examination of the injury mechanism, medical imaging techniques such as magnetic resonance imaging (MRI) and ultrasound imaging (US) are gaining popularity for assistance with both diagnoses and prognoses. These imaging techniques provide valuable structural and physiological information that is provides more insight into the nature and extent of the damage to guide image treatment. Currently, MRI is the gold standard for use with musculoskeletal applications, but US is becoming more widespread due to its affordability, portability, and real-time imaging capabilities.

Ultrasound elastography (USE) is a family of techniques that are used to allow the visual analysis and quantification of the mechanical properties of soft tissue. Injury induced changes in muscle structure affect the mechanical properties of the tissue, and can be detected using USE. Since the echogenicity of a tissue is not directly related to its mechanical properties, ultrasound elastography can extract important information about tissue stiffness and deformability that might not otherwise be attainable. Such mechanical information is especially useful in distinguishing between fibrotic tissue and

fatty infiltration. The goal of this thesis is to develop USE as an affordable, fast, and readily available alternative to MRI for early stage diagnosis of acute muscle injury.

In pursuit of this goal, we first developed a technique to obtain repeatable and reproducible strain images using USE. We found that a simple averaging procedure performed on 4-8 repeated USE compression cycles significantly improved both the reproducibility and repeatability of the resulting strain images compared to strain images generated using an automated USE system. We then showed that USE combined with principal component analysis can be used to quantify and locate muscle injury in a finite element model, and can feasibly be applied to strain images generated using USE. Finally, we attempted to use the procedures developed in the first two studies to detect and monitor contusion injury in a rat model. However, due to equipment limitations, the results of this study were inconclusive. This thesis is concluded by a summary of the overall findings and discussion of future work.

BIOGRAPHICAL SKETCH

Matthew Joseph (Matt) Leineweber earned his Bachelor of Science degree in Mechanical Engineering the University of Portland in Portland, OR in 2009. He subsequently joined the doctoral program in Mechanical Engineering at Cornell University in 2009 and has since earned his Master of Science degree in Mechanical Engineering in 2012.

Matt has been the recipient of the Cornell Graduate Student Fellowship and Graduate Research Fellowship, as well as a two-time Honorable Mention for the National Science Foundation Graduate Research Fellowship. In addition to his research experiences, Chi has been the teaching assistant of three courses over five semesters in the department of Mechanical Engineering. In the spring semester 2014 he was awarded the Mechanical Engineering Department Teaching Assistant award for excellence in teaching.

Outside of his research and teaching experiences, Matt took an active part in the Mechanical Engineering graduate community. He served as President of the Sibley Graduates in Mechanical and Aerospace Engineering (SiGMA) for two years, and captained many of the intramural sports teams throughout his graduate school tenure. Matt is proud to say that after five years and several missed opportunities, the MAE Fighting Reuleaux finally won their intramural softball championship.

Matthew Joseph Leineweber's dissertation was supervised by Dr. Yingxin Gao, PhD.

To Karen. You are the best thing to come out of graduate school. Thank you for putting up with my shenanigans, complaints, dreams, and whims. You are my best friend and love of my life.

ACKNOWLEDGMENTS

First I would like to thank my adviser, Professor Yingxin Gao, for all of her continuous support, encouragement, and mentorship throughout my graduate studies. Her door was always open to discuss research, coursework, and life in general, and she was always looking to make sure we had what we needed to succeed. I have been privelaged to have her as an adviser and friend.

Additionally, thank you to Professors Hernandez and Reeves, my PhD committee members for their guidance and help in research and teachings. I would also like to thank the Department of Mechanical Engineering and the Graduate School of Cornell University for their financial support.

This dissertation and the work that led to it would not have been possible without the support of Marcia Sawyer and Judy Thoroughman. Their guidance and help with the graduate school procedures kept me on track, and their continuous support of the MAE graduate community helped keep fed, entertained, and mostly sane.

Thank you to my labmates, Natasha, Radhika, Shama, and Amy for all of their help, support, and friendship through the years. Thank you to Julia Westborn for all of her help on research projects and putting up with me as a mentor.

A huge thanks to all of my friends at Cornell. We truly had a unique and special incoming class. I will always remember our roving band of 50+ engineers taking restaurants and bars by storm, and later the BBQ's, wine tours, parties, and relaxing nights. Thanking you all individually would double the size of this thesis. Suffice to say, you all made this amazing experience what it was. I couldn't have done it without you.

Finally, thank you to my family who has always been there to support and encourage me to push my limits, especially during the most difficult times.

TABLE OF CONTENTS

LIST OF ABBREVIATIONS

CNR – Contrast-to-noise ratio

CT – Computed Tomography

DOMS – Delayed Onset Muscle Soreness

ECM – Extracellular matrix

FE – Finite Element

MRI – Magnetic Resonance Imaging

PCA – Principal Component Analysis

PET – Positron Emission Tomography

QSE – Quasi-static ultrasound elastography

RF – Radiofrequency

RM – Relative Magnitude

US – Ultrasound

USE – Ultrasound Elastography

CHAPTER 1

INTRODUCTION

1.1 Skeletal Muscle Injury – A Motivation

Skeletal muscle injuries are frequent in sports and exercise, accounting for between 20-55% of all sports injuries [1–3]. In the broadest sense, these injuries can be classified as either functional or structural-mechanical in nature [2]. Functional injuries refer to minor fatigue-induced injuries, such as delayed-onset-muscle-soreness (DOMS), where structural-mechanical injuries refer to those that disrupt or cause damage to the muscle fibers or fascicles [2,4]. 90% of injuries categorized as structural-mechanical are either muscle strains or contusions [5,6]. Strain injuries are caused by high internal tensile forces in the muscle. Their severity can range from mild to severe, with the worst cases resulting in full rupture of the myofibers and/or the surrounding connective tissue [1]. Contusion injuries are the result of sudden blunt-force trauma to the tissue. Such injuries are usually compressive, or crushing, in nature, and primarily occur in the muscle belly [1,7,8]. Unlike strains, contusion injuries are not intrinsic to the nature of the exercise, rather they are caused by external forces.

Muscle injuries are primarily diagnosed through symptomatology and understanding of the injury mechanism, with only the most severe cases requiring radiologic assistance [3,9]. However, magnetic resonance imaging (MRI) and, more recently, ultrasound are being recognized as valuable for confirming diagnoses and determining prognoses. These imaging techniques provide valuable structural and physiological information that provides more insight into the nature and extent of the damage to guide image treatment [10].

1.2 Skeletal Muscle – Structure and Function

Of the three types of muscle tissue: cardiac muscle, smooth muscle, and skeletal, or striated, muscle; skeletal muscle is the most prevalent, accounting for between 40-50% of total body weight [22]. The primary role of skeletal muscle is to generate force and produce motion of the skeletal system. This force generation capability is unique to muscle tissue, and differentiates it from other musculoskeletal tissues such as ligament and tendon. Skeletal muscle is even more specialized in that the force generation is voluntary. That is, unlike cardiac or smooth muscle, the conscious brain has control over whether a muscle is activated or not. Both the passive mechanical properties, which are determined by the tissue structure, and active mechanical properties, which are dependent on nervous stimulation, are crucial to the function of skeletal muscle.

Skeletal muscle has a hierarchical structure composed of three concentric layers: muscle fibers, muscle fascicles, or bundles, and muscle tissue. Each of these layers is encompassed in connective tissue. Muscle fibers are the fundamental layer, and are comprised of long, cylindrical multi-nucleate cell. These cells are made up of myofibrils, which are the key components in the contractile function of muscle. Each myofibril is comprised of functional units, called sarcomeres, which are arranged in parallel to form a banding pattern along the muscle fiber. Sarcomeres are composed of thick and thin filaments, called actin and myosin, which slide relative to one another to generate force. A process known as the *cross-bridge* cycle controls the attachment and detachment of actin and myosin to produce this force and motion. Muscle fascicle, or bundles, are groups of muscle fibers surrounded by a sheath of muscle tissue. These fascicles are further bundled together to form the bulk muscle tissue.

The aforementioned connective tissue wrapping each muscle layer is called the

extracellular matrix (ECM), and is the other main component of skeletal muscle tissue. There are three different structural levels of the ECM: the endomysium surrounds the single myofibers; the perimysium binds the muscle fascicles; and the epimysium encompasses the entire skeletal muscle (Figure 1.1). The ECM not only provides structural support to ensure integrity of the whole muscle, but more importantly, interactions between the ECM and myofibers determine the mechanical behaviors of skeletal muscles [24–29].

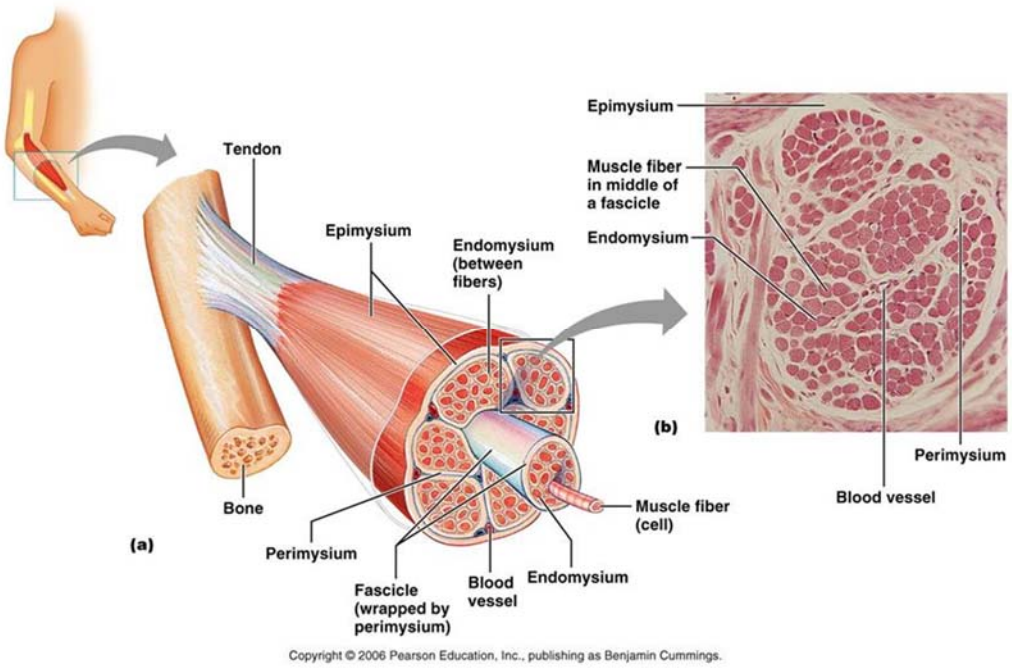

Figure 1.1. A schematic of the hierarchical structure of skeletal muscle. The extracellular matrix, including the endomysium that surrounds the single muscle fiber, the perimysium surrounding the fascicle, and the epimysium surround the whole muscle. Adapted from Essentials of Human Anatomy and Physiology with permission from Pearson Education © 2006 [30].

1.3 Muscle Imaging Techniques – A Case for Ultrasound

MRI is currently the gold standard for musculoskeletal imaging [7,10,11], primarily due to its high-quality anatomic images. However, ultrasound is gaining clinical popularity as both a supplement and, in some cases, alternative to MRI for musculoskeletal applications [10,12,13]. Compared to MRI, ultrasound has the advantages of being fast, portable, inexpensive, and can record images in real-time, allowing for functional and dynamic assessment of the muscles and tendons [10]. Furthermore, many current ultrasound systems can achieve significantly higher spatial resolution compared to clinical MRI, making them preferable for examining small detailed structures, such as tendons, ligaments, or small muscles. However, these ultrasound advantages come at the cost of decreased image clarity. Ultrasound images are often noisy and difficult to interpret compared to the clearly defined regions and structures possible using MRI, which can be seen in Figure 1.2 below.

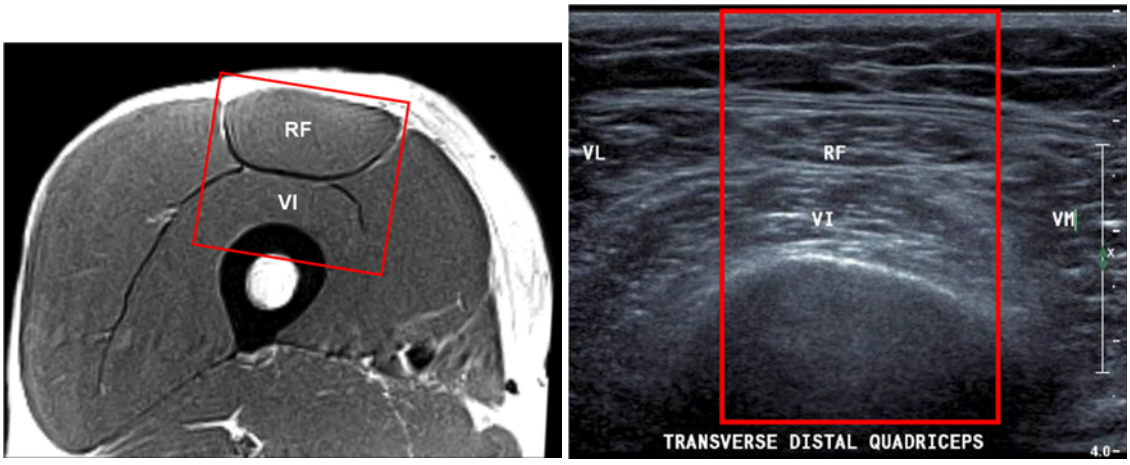

(a) (b)

Figure 1.2: (a) MRI and (b) ultrasound images of the anterior thigh are shown. The red rectangle represents approximately the same region of interest in each image. The anatomy of the thigh is clearly distinguishable in the MRI image, with the rectus femoris (RF) and vastus intermedialis (VI) muscles easily identified. The muscles can still be seen in the ultrasound image, but the borders are not as easily identified. Furthermore, only a small region of the thigh can be seen at one time in the sonogram, with the bone obstructing the imaging of any deeper structures.

The low cost, portability, and real-time imaging capabilities of ultrasound make it particularly well suited for use with muscle injury. Ultrasound systems are commonly used in small clinics, and with the advent of portable ultrasound units (Sonosite, GE, Philips, etc.) they can be brought on-site to sporting events and gyms. Rather than waiting for a MRI to become available, clinicians and trainers can use ultrasound images to assist in injury diagnosis earlier, thereby enabling faster treatment and improving the likelihood of a shorter healing time. In addition to the increased availability of ultrasound, its real-time capabilities allow for imaging of muscle function. Since skeletal muscle is intrinsically dynamic, visualizing how the tissue is deforming during motion can provide important information about muscle health. For example, scar tissue formed after injury can hinder tissue motion and alter the functional dynamics of the muscle [10,14]. Real-time Doppler imaging can also be used to identify areas of increased or decreased blood flow that can give insight into possible areas of muscle damage or regeneration[15].

Finally, the real-time capabilities of ultrasound also allow for visualization and quantification of the mechanical behavior of soft tissues through ultrasound elastography (USE). Briefly, this process, which will be expounded upon later, relies upon mechanical deformation of the tissue of interest in conjunction with real-time ultrasound imaging of the resulting internal deformations. Using this deformation data, the tissue strain is calculated and used to identify areas variable mechanical properties, such as stiffness. Since muscle injury often causes structural changes to the tissue, the resulting changes in mechanical behavior may provide important insights into the nature of the injury [16–18].

1.4 Basic Ultrasound Physics – An Overview

Unlike other imaging modalities, such as x-ray, x-ray computed tomography (CT), and positron-emission-tomography (PET), which use ionizing radiation, or electromagnetic energy (used in MRI), ultrasound imaging consists solely of non-ionizing high-frequency sound waves. For clinical imaging, these waves are usually in the 5-12 MHz range. The basis for ultrasound imaging centers on emitting waves at ultrasonic frequencies and receiving the echoes.

At its most fundamental level, ultrasound imaging is simply a pulse-echo system. That is, sound energy is emitted into a medium, usually soft tissue, and then transmitted, reflected, and scattered as it propagates away from the source. For ultrasound imaging, these reflections are most important, as they occur at interfaces between different media, "bouncing" back towards the receiver. The intensity and time-of-flight of these echo signals contain important information about the distance between source and interface, as well as the degree of dissimilarity between the interfacing media. As such, ultrasound images are primarily density maps, with large reflections occurring at surfaces between highly dissimilar media [19].

The source of the ultrasonic signal is usually a piezoelectric crystal, which convert electronic signals into mechanical vibrations, and vice-versa. Excitation signals are sent to the piezoelectric crystals, causing them to vibrate and emit energy. Immediately after they are excited, the crystals are allowed to vibrate freely in response to the echoes of the original signal. As the echoes cause the piezoelectrics to vibrate, they induce a voltage difference that can be recorded by the receiver system. These crystals can be excited as a single element, resulting in a single pulse-echo signal, or A-line. However, they are more often, as a group of elements in a linear array. The apparatus that contains

the piezoelectric crystals is referred to as a *transducer*.

Once the ultrasonic pulse is generated by the transducer, it act as a mechanical disturbance that propagates through the media the transducer is in contact with. The propagation speed depends on the media as a function of density. Air, for example, has a propagation speed $c = 331\ m/s$ while most soft tissues are around $c = 1540\ m/s$ [19]. Since the piezoelectrics immediately switch from 'send' to 'receive' mode, the time between a signal's emission and a reflection is known, which is directly proportional to the distance from source to reflective surface

$$d = \frac{1}{2}ct,$$

where d is the spatial distance between the transducer and echo surface, and t is the time-of-flight of the signal. The factor of $1/2$ accounts for the "down and back" propagation of the pulse. Therefore, the temporal data recorded by the ultrasound system can be translated into spatial data, which is more useful for imaging purposes.

For a single A-line, the theoretical resolution is limited by the pulse length, which is dependent on the center frequency, f (usually in the 5-12 MHz range), temporal pulse duration, Δt, and propagation speed, c. The lower limit for resolution along the beam path is half the spatial pulse length, and higher resolutions can be achieved with higher center frequencies, as illustrated in Figure 1.3. However, higher frequencies are more likely to be absorbed by the tissue, resulting in significant attenuation. Thus, there is a trade-off between imaging depth and achievable resolution [19].

All of the above calculations are only useful for the direction of beam propagation, that is, for a single A-line. However 2D images require multiple A-lines in parallel. These images are usually created using linear-array transducers, which fire pulses sequentially

along the array. The lateral resolution is determined by the width of the focused beam, which is a function of the number of elements being activated. As such, the lateral resolution is significantly less than that of the axial direction. While axial resolution can easily reach 100 μm or less, lateral resolutions are not typically smaller than a few millimeters [19–21].

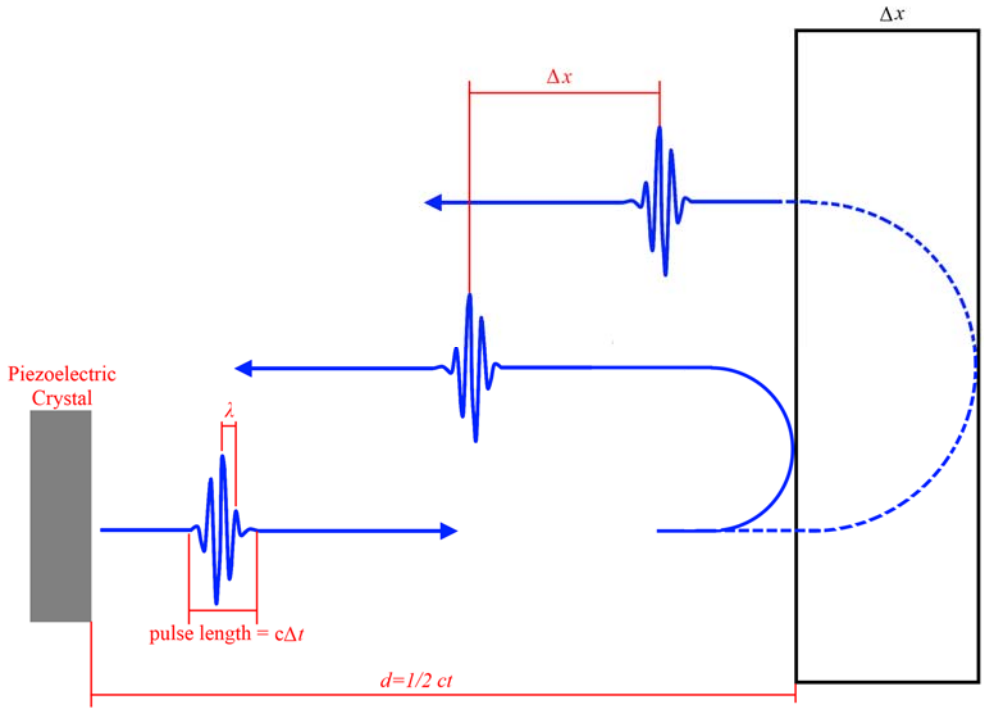

Figure 1.3: When an ultrasound pulse is emitted by the piezoelectric crystal, it travels through soft at the speed of sound,c, through the tissues. The time,t, that it takes a signal to make a "round-trip" after being emitted is related to the distance between source and reflection surface, d. When the pulse encounters a tissue interface, its energy is partially reflected and transmitted. Ultrasound signals reflecting from surfaces separated by distance Δx will experience a relative delay. The returning pulses can only be distinguished from one another if the separation between the two surfaces is greater than half the ultrasound pulse length $\Delta x \geq 1/2\ c\Delta t$.

Since 2D B-mode images are essentially series of A-lines in parallel, the achievable frame-rates of real-time ultrasound imaging depend on the both the imaging depth and number of A-lines (image width) required. Larger images take more time to acquire,

resulting in slower frame-rates. Typical ultrasound systems using 128 element transducers can achieve approximately 30 frames per second. Higher frame rates are available for detailed imaging of superficial tissues, or coarse-resolution imaging of deeper structures.

1.5 Ultrasound Elastography – Principles and Applications to Musculoskeletal Tissues

Ultrasound elastography (USE) is a family of techniques that are used to allow the visual analysis and quantification of the mechanical properties of soft tissue. The earliest USE methods were developed in the early 1990's, and several methods have since developed to allow for *in-vivo* examination of internal strain distributions, which provide information about tissue stiffness. The basic principle of USE is to mechanically deform a soft tissue, and record the resulting deformation in real-time using ultrasound imaging techniques [16–18]. While the deformation mechanisms vary widely between different USE techniques, including surface vibration [31,32], acoustic deformation [33,34], and shear waves [35–37], the oldest and most commonly used method simply uses the transducer to apply a surface pressure to the tissue [16,34,38]. This final technique is referred to as quasi-static ultrasound elastography (QSE).

The displacement maps generated using QSE can be used to calculate the strain within the tissue. Visual inspection of these strain maps can identify local regions of increased or decreased deformation that correspond to areas of variable tissue stiffness. Since the tissue mechanical properties are independent of its acoustic properties, QSE provides additional information about the muscle structure that would not otherwise be available [18,39,40]. Figure 1.4 illustrates this principle. For example, Traditionally, QSE has been used for finding tumors within a soft tissue, since they are often much harder than their surroundings.

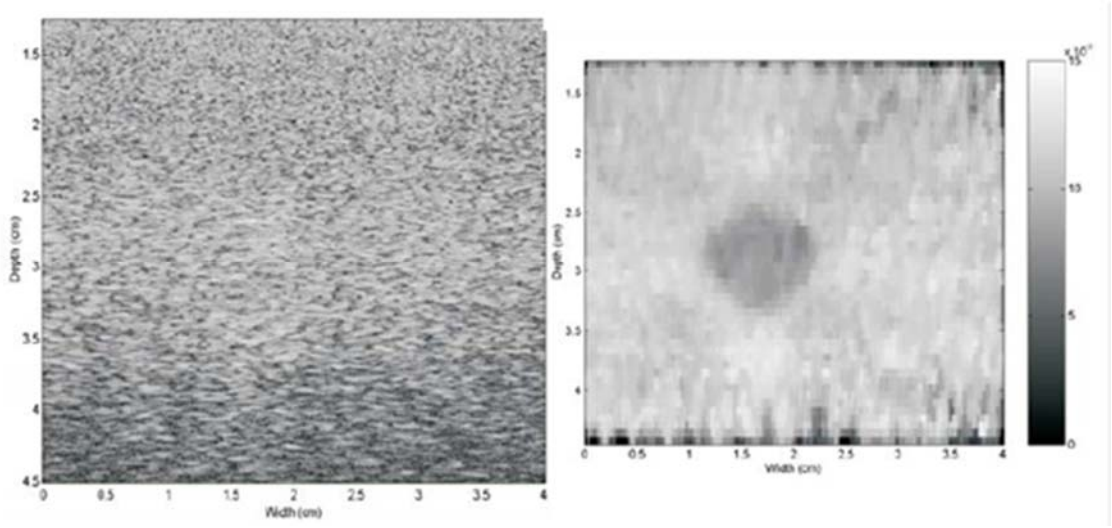

(a) (b)

Figure 1.4: (a) B-mode image and (b) elastogram of a test phantom with a local region of increased stiffness. The stiff region cannot be seen in the sonogram, but is readily available in the strain image generated using compression QSE. Reproduced with kind permission from Dynamedia, Inc © 2002 [41].

Recently, USE has been gaining momentum for use with musculoskeletal tissues. Both musculoskeletal disease and injury result in changes to the mechanical properties of the tissues, which can be visualized using USE. Although several differing elastography techniques have been used with musculoskeletal tissues in the literature, QSE is the cheapest and most widespread. The recent introduction of QSE capabilities into

clinically available ultrasound systems has made it more desirable as both a clinical and research tool for musculoskeletal applications [18].

The striated pattern of tendons, ligaments, and muscles often result in distinctive strain patterns. Tendons, for example, are the most widely studied of these three tissue types, and have been shown to have two distinct strain patterns: homogeneously hard or very inhomogeneous with longitudinal bands of softer tissue [42]. While some striated patterns can be seen in the B-mode images, these bands of decreased stiffness are much more pronounced and were not seen to change with changes in the B-mode images. There is significantly less data on USE applied to skeletal muscle. Although the strain maps of muscle tissue have not been extensively studied, relaxed healthy muscles seem to exhibit inhomogeneous mosaics of soft tissue with areas of increased stiffness near muscle boundaries (Figure 1.5) [43,44]. However, the mechanisms behind these increases are not well understood, nor are normal variations in strain patterns between muscles and individuals [18].

Although few in number, applications of USE to skeletal muscle pathologies have shown promising results for identifying changes in mechanical properties resulting from muscle damage. For example, muscle fatigue due to prolonged contractions, such as may be experienced during exercise, has been shown to affect the viscoelastic properties of the tissue [45,46]. Similarly, a study following the regeneration of skeletal muscle after inflammatory myositis showed stiffness changes over the healing process due to fibrosis and fatty infiltration [43]. However, applications of USE to examining the effects of acute muscle injury, such as contusion or strains, have only been minimally explored, and the effects of these injuries on the tissue mechanical properties are not

well understood.

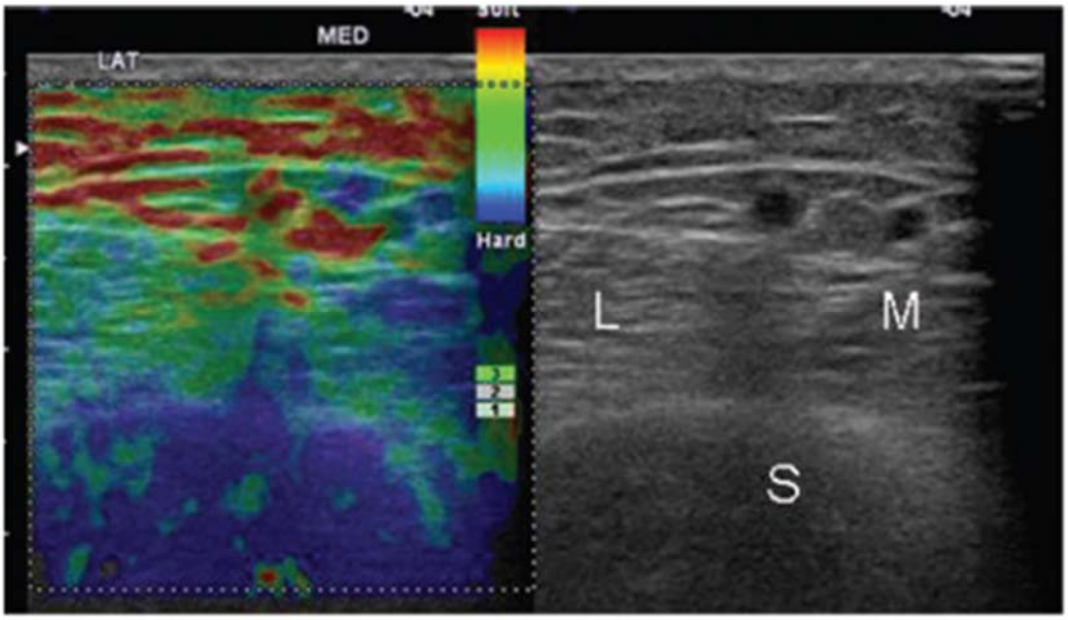

Figure 1.5: A sonogram of the relaxed calf muscles of a healthy human is shown (right) along with a strain image generated using commercially available software.. The lateral and medial heads of the gastrocnemius(L and M) are shown, as is the soleus (S). These regions show a mosaic of medium-high stiffness. The red areas in the strain image (elastogram) mostly correspond to subcutaneous fat, showing increased strain magnitudes (softer tissue). The decreased strain magnitudes in the soleus are most likely due to loss of signal due to the depth of the muscle. Reprinted with kind permission from the British Institute of Radiology © 2012[18].

1.6 Specific Aims

The overall goal of this thesis was to develop ultrasound elastography as an affordable, fast, and readily available alternative to MRI for early stage diagnosis of acute muscle injury. Since USE is highly operator-dependent and prone to both intra- and inter-operator error, completion of this goal first required an understanding of how to minimize these user-effects. Both experimental and computational studies are used to examine the effects of operator error on elastograms of skeletal muscle, both for healthy

and injured tissue, as well as how these errors can be overcome to accurately locate and quantify damaged tissue. Three specific aims are addressed in pursuit of this goal: (1) Establish a procedure to account for intra-subject error, (2) examine the feasibility of principal component analysis for improving inter-subject reproducibility, and (3) apply QSE to healthy and injured skeletal muscle to characterize tissue damage during the healing process.

1.6.1 Averaging Improves Strain Images of the Biceps Brachii Using QSE

The aim of this chapter is to describe a procedure by which artifacts and errors introduced by intra-subject variation and operator error can be minimized. Rather than attempting to eliminate the sources of these operator errors, namely improper transducer positioning, inconsistent compressions, and transducer shaking, a simple averaging procedure was performed on the resulting strain images to smooth the effects of these errors. Repeated QSE scans of the *biceps brachii* of young and healthy humans were performed using both manual and automated compression techniques. The effects of averaging different numbers of scans for each subject were explored in comparison to using automated QSE techniques to reduce the possible sources of error.

1.6.2 Applying Principal Component Analysis to Identify Muscle Injury Using QSE

Even after repeatable and reproducible strain images are possible, successful diagnosis requires inter-subject comparison of strain images. As such, the effects of individual muscle variations in mechanical properties and potential operator differences need to be addressed. Principal component analysis (PCA) has been shown to be feasible in diagnosing areas of damaged tissue in simulated tendon elastograms. This efficacy of this technique applied to skeletal muscle is explored with finite element models of skeletal muscle undergoing compression. The model input parameters are varied to

simulate both operator and individual muscle variability, and the resulting displacement and strain maps are analyzed using PCA. Finally, PCA is applied to a small dataset of experimental ultrasound data to characterize its feasibility for use with physical muscle.

1.6.3 Using QSE to Characterize Muscle Health After Contusion Injury

Once a reliable imaging procedure has been established, QSE can be used to identify both global and local injury-induced changes in mechanical properties. Functional testing can be used to determine muscle health at time-points before and after injury. Performing QSE at each of these time-points allows for direct correlation between muscle health and mechanical properties. The mechanical information yielded by QSE can complement standard ultrasound images, as well as provide additional information about tissue type and integrity.

1.7 Chapter Overviews

To accomplish each of the specific aims, a detailed understanding of skeletal muscle structure and function, injury mechanisms, basic ultrasound physics, and ultrasound elastography techniques are required. These topics have been introduced and discussed in some detail in Chapter 1.

Chapter 2 describes a procedure to minimize the effects of intra-operator variation on strain images of the *biceps brachii* generated from QSE. Both freehand and automated compressions were performed on the *biceps brachii* of nine young and healthy subjects. An averaging procedure is introduced to minimize the effects of operator error without the need for additional equipment to stabilize the compression process. Repeated compressions of are performed and the resulting strain images averaged to smooth the artifacts introduced during QSE. The effects that the number of scans included in the

average have on the repeatability and reproducibility of the images are explored.

The purpose of Chapter 3 is to test the feasibility of PCA and the "damage-displacement" technique for characterizing healthy displacement images and identifying damaged tissue regions after injury. In this chapter, finite element models of both healthy and contused skeletal muscle are used to test this feasibility. PCA is performed on simulated displacement images output by the healthy finite element models to determine the major sources of variation caused by operator error and inter-subject variability in muscle stiffness.

In Chapter 4, QSE is applied to a rat contusion-injury model to characterize the mechanical properties of the gastrocnemius muscle before and after injury. Muscle functional torque tests are used to determine muscle health at various time-points before and after injury. QSE is then performed on the muscle at each of these time points to examine how strain distributions within the muscle are affected by injury and the healing process. These strain distributions in conjunction with traditional ultrasound imaging techniques can provide insight into how the muscle structure and composition change during regeneration after contusion injury.

Finally, Chapter 5 summarizes the most important conclusions of the thesis, and directions of future research are proposed. Additional information supplemental to these chapters is included in the Appendix.

REFERENCES

1. Järvinen T, Järvinen M, Kalimo H. Regeneration of injured skeletal muscle after the injury. Muscles, ligaments …. 2013;3(grade II):337–45.

2. Ekstrand J, Hägglund M, Waldén M. Epidemiology of muscle injuries in professional football (soccer). Am J Sports Med. 2011 Jun;39(6):1226–32.

3. Valle X. Clinical practice guide for muscular injuries: epidemiology, diagnosis, treatment and prevention. Br J Sports Med. 2011 Jan 20;45(2):e2–e2.

4. Saartok T. Muscle injuries associated with soccer. Clin Sports Med. 1998;17(4):811–7.

5. Beiner JM, Jokl P, Cholewicki J, Panjabi MM. The effect of anabolic steroids and corticosteroids on healing of muscle contusion injury. Am J Sports Med. 1999;27(1):2–9.

6. Delos D, Leineweber MJ, Chaudhury S, Alzoobaee S, Gao Y, Rodeo S a. The Effect of Immediate and Delayed Injection of Platelet-Rich Plasma (PRP) on Muscle Contusion Healing in the Rat. Orthop J Sport Med. 2013 Sep 20;1(4 Suppl):2013–5.

7. Douis H, Gillett M, James SLJ. Imaging in the diagnosis, prognostication, and management of lower limb muscle injury. Semin Musculoskelet Radiol. 2011 Feb;15(1):27–41.

8. Crisco JJ, Hentel KD, Goehner K, Jokl P, Haven N. Maximal contraciton lessens impact response in a muscle contusion model. Science (80-). 1996;29(10):1291–6.

9. Noonan TJ, Garrett WE. Muscle strain injury: diagnosis and treatment. J Am Acad Orthop Surg. 1999;7(4):262–9.

10. Woodhouse JB, McNally EG. Ultrasound of skeletal muscle injury: an update. Semin Ultrasound CT MR. Elsevier Inc.; 2011 Apr;32(2):91–100.

11. Ringleb SI, Bensamoun SF, Chen Q, Manduca A, An K-N, Ehman RL. Applications of magnetic resonance elastography to healthy and pathologic skeletal muscle. JMRI - J Magn Reson Imaging. 2007 Mar;25(2):301–9.

12. Chifishman G. Ultrasound imaging distinguishes between normal and weak muscle1. Arch Phys Med Rehabil. 2004 Jun;85(6):980–6.

13. Peetrons P. Ultrasound of muscles. Eur Radiol. 2002;12(1):35–43.

14. Hodges PW, Pengel LHM, Herbert RD, Gandevia SC. Measurement of muscle contraction with ultrasound imaging. Muscle Nerve. 2003 Jun;27(6):682–92.

15. Campbell SE, Adler R, Sofka CM. Ultrasound of muscle abnormalities. Ultrasound Q. 2005;21(2):87–94; quiz 150, 153–4.

16. Ophir J, Cespedes I, Ponnekanti H, Yazdi Y, Li X. Elastography: a quantitative method for imaging the elasticity of biological tissues. Ultrason Imaging. 1991;13(2):111–34.

17. Sarvazyan A, Hall TJ, Urban MW, Garra BS. An Overview of Elastography - An emerging branch of medical imaging. Curr Med Imaging Rev. 2012;7(4):255–82.

18. Drakonaki EE, Allen GM, Wilson DJ. Ultrasound elastography for musculoskeletal applications. Br J Radiol. 2012 Nov;85(1019):1435–45.

19. Wolbarst AB. Physics of Radiology. Second. Madison, Wisconsin: Medical Physics Publishing; 2005.

20. Chen L, Housden J, Treece GM, Gee H. A Hybrid Displacement Estimation Method for Ultrasonic Elasticity Imaging. IEEE Trans Ultrason Ferroelectr Freq Control. 2010;57(4):866–82.

21. Konofagou E, Ophir J. A new elastographic method for estimation and imaging of lateral displacements, lateral strains, corrected axial strains and Poisson's ratios in tissues. Ultrasound Med Biol. 1998;24(8):1183–99.

22. Lorenz T, Campello M. Biomechanics of Skeletal Muscle. In: Nordin M, Frankel V, editors. Basic biomechanics of the musculoskeletal system. 3rd ed. Philadelphia: Lippincott Willams & Wilkins; 2001. p. 148–71.

23. Widmaier EP, Raff H, Strang KT. Vander's Human Physiology: The Mechanisms of Body Function. 11th ed. New York, NY: the McGraw-Hill Company; 2008.

24. Gao Y, Kostrominova TY, Faulkner JA, Wineman AS. Age-related changes in the mechanical properties of the epimysium in skeletal muscles of rats. J Biomech. 2008;41(2):465–9.

25. Gao Y, Waas AM, Winema AS. Mechanics of Injury to Muscle Fibers. J Mech Med Biol. 2007;7(4):381–94.

26. Gao Y, Winema AS, Waas AM. Time-dependent lateral transmission of force in skeletal muscle. Proc R Soc A. 2009;465(2108):2441–60.

27. Zhang C, Gao Y. Finite element analysis of mechanics of lateral transmission of force in single muscle fiber. J Biomech. 2012/06/12 ed. 2012;45(11):2001–6.

28. Purslow PP. Muscle fascia and force transmission. J Bodyw Mov Ther. 2010;14:411–7.

29. Purslow PP, Duance VC. Structure and function of intramuscular connective tissue. In: Hukins DWL, editor. Connective Tissue Matrix. Boca Raton: CRC Press; 1990. p. 127–66.

30. Marieb EN. Essentials of Human Anatomy & Physiology. Eighth. San Francisco, California: Pearson; Benjamin Cummings; 2006.

31. Hoyt K, Kneezel T, Castaneda B, Parker KJ. Quantitative sonoelastography for the in vivo assessment of skeletal muscle viscoelasticity. Phys Med Biol. 2008;53(15):4063–80.

32. Shinohara M, Sabra K, Gennisson J-L, Fink M, Tanter M. Real-time visualization of muscle stiffness distribution with ultrasound shear wave imaging during muscle contraction. Muscle Nerve. 2010 Sep;42(3):438–41.

33. Faquin L, Luo Y, Ban Y, Wu R, Tian J, Yu T, et al. Muscle crush injury of extremity: quantitative elastography with supersonic shear imaging. Ultrasound Med Biol. 2012 May;38(5):795–802.

34. Lindop JE, Treece GM, Gee AH, Prager RW. 3D elastography using freehand ultrasound. Ultrasound Med Biol. 2006 Apr;32(4):529–45.

35. Deffieux T, Gennisson JL, Tanter M, Fink M. Ultrafast imaging of in vivo muscle contraction using ultrasound. Appl Phys Lett. 2006;89:184107.

36. Deffieux T, Gennisson JL, Tanter M, Fink M. Ultrafast imaging of in vivo muscle contraction using ultrasound. Appl Phys Lett. 2006;89:184107.

37. Deffieux T, Gennisson J-L, Tanter M, Fink M. Assessment of the mechanical properties of the musculoskeletal system using 2-D and 3-D very high frame rate ultrasound. IEEE Trans Ultrason Ferroelectr Freq Control. 2008 Oct;55(10):2177–90.

38. Doyley MM, Bamber JC, Fuechsel F, Bush NL. A freehand elastographic imaging approach for clinical breast imaging: system development and performance evaluation. Ultrasound Med Biol. 2001;27(10):1347–57.

39. Parker K, Lerner R. Sonoelasticity of organs: shear waves ring a bell. J ultrasound Med. 1992;

40. Hiro T, Leung CY, Guzman S De, Caiozzo VJ, Farvid AR, Karimi H, et al. Imaging / Diagnostic Testing assessment of mechanical properties in human. 1997;133(1):11–4.

41. Varghese T, Zagzebski J, Frank G, Madsen EL. Elastographic imaging using a handheld compressor. Ultrason Imaging. 2002 Jan;24(1):25–35.

42. Drakonaki EE, Allen GM, Wilson DJ. Real-time ultrasound elastography of the normal Achilles tendon: reproducibility and pattern description. Clin Radiol. The Royal College of Radiologists; 2009 Dec;64(12):1196–202.

43. Botar-Jid C, Damian L, Dudea SM, Vasilescu D, Rednic S, Badea R. The contribution of ultrasonography and sonoelastography in assessment of myositis. Med Ultrason. 2010 Jun;12(2):120–6.

44. Drakonaki EE, Allen GM. Magnetic resonance imaging, ultrasound and real-time ultrasound elastography of the thigh muscles in congenital muscle dystrophy. Skeletal Radiol. 2010 Apr;39(4):391–6.

45. Witte RS, Kim K, Martin BJ, O'Donnell M. Effect of fatigue on muscle elasticity in the human forearm using ultrasound strain imaging. Conf Proc IEEE Eng Med Biol Soc. 2006 Jan;1:4490–3.

46. Niitsu M, Michizaki A, Endo A, Takei H, Yanagisawa O. Muscle hardness measurement by using ultrasound elastography: a feasibility study. Acta radiol. 2011 Feb 1;52(1):99–105.

CHAPTER 2

AVERAGING IMPROVES STRAIN IMAGES OF THE BICEPS BRACHII USING QUASI-STATIC ULTRASOUND ELASTOGRAPHY[1]

2.1 Introduction

Damage to skeletal muscle tissue, such as contusions, tears, and strains, account for approximately 90% of all sports related injuries[1]. Although magnetic resonance imaging (MRI) is currently the gold standard for diagnostic imaging of soft tissue, ultrasound is recognized as a viable alternative for soft tissue imaging, due to its portability, affordability, and ability to capture sequences of images in real time [2,3]. Quasi-static elastography takes advantage of ultrasound's unique ability to capture image sequences to track tissue deformation, and has emerged as a potential diagnostic tool to monitor musculoskeletal pathologies [4].

Quasi-static elastography (QSE) operates on the principle that when tissue is externally compressed, the resulting deformation depends on the mechanical properties of the tissue [5]. Accordingly, this technique tries to recover information about the mechanical properties from information about tissue deformation. Ultrasound elastography is shown to detect lesions in breast tissue and fibrosis in liver tissue [6–9], measure intravascular elasticity [10,11], as well as an ability to estimate strain in tendons [12–14]. QSE could also potentially be used to identify regions of damaged or abnormal tissue in skeletal muscle, but there are few studies exploring these applications[4].

[1] Leineweber, MJ. Westborn, J. Cochran, A. Choi, J. Gao, Y. "Averaging Improves Strain Images of the *Biceps brachii* Using Quasi-Static Ultrasound Elastography", *British Journal of Radiology*, April 2014. (accepted)

The primary limitation of quasi-static elastography is its dependence on consistent and steady ultrasound images to create quality strain images. Image steadiness is particularly important with musculoskeletal tissues due to their anisotropic and inhomogeneous structure. Variability in image collection, inherent to the nature of freehand manipulation of the ultrasound transducer, results in changes in the imaging window and unsteady application of force during a single compression, as well as variations in the rate, magnitude, and direction of loading between trials. These inconsistencies may lead to large errors in the resulting strain images, directly affecting the accuracy and repeatability of strain measurements. For example, transducer misalignment alone has been shown to result in strain measurement errors as high as 23% [15]. To mitigate variation between examinations and measurement error, a number of studies have developed scanning systems that assist the operator while examining the tissue of interest. These automated and assisted systems have employed various mechanical compression and feedback techniques to successfully reduce extraneous transducer motion and improve the resulting strain images [16–18]. However, these enhancements do come at the cost of added training and expensive, often cumbersome equipment.

Rather than attempting to eliminate the aforementioned sources of measurement error themselves, it may be possible to minimize the imprecision of the strain images through a simple averaging procedure, wherein multiple ultrasound compression-scans are performed, and the resulting strain images averaged to create a single representative image.

Although averaging is expected to improve repeatability in the strain images, currently, there is no literature employing such averaging techniques to musculoskeletal

elastography. Instead, multiple compressions are performed, and the result of a single scan is selected from amongst the set to be further analyzed [13,14,19]. Several questions about the approach of averaging need to be addressed, including: (1) can it achieve similar strain image repeatability as automated scans? (2) Does it require too many scans to achieve acceptable repeatability? (3) Will averaging actually remove important data in the image that are unique to the patient and are needed to properly characterize the tissue health?

In this paper, we determine whether averaging strain-images from repeated scans of the *biceps brachii* reduces the effects of variability in ultrasound images. Specifically, we tested three hypotheses: (1) the final images created by averaging strain images over multiple manual scans are both qualitatively and quantitatively similar to strain images resulting from automated compression procedures; (2) averaging over multiple scans increases the repeatability of the resulting strain images compared to single automated compressions; (3) the averaged strain images from a single subject will be more reproducible between operators than strain images from a single freehand scan.

2.2 Materials and Methods

All testing procedures were performed with approval from the Cornell University Institutional Review Board (IRB). Nine healthy volunteers, 5 male and 4 female, 26.4 ± 3.2 (mean ± SD) years old were recruited from Cornell University. Participants selected were asked to fill out a questionnaire about their health history to ensure did not have any history of musculoskeletal diseases or injury to the *biceps brachii*. All participants underwent ultrasound imaging of the dominant arm *biceps brachii*. Participants provided informed consent prior to their involvement in the study.

This section details the procedure used to (1) create averaged strain images from multiple compressions of the *biceps brachii*, as well as (2) test the accuracy (similarity to automated images), repeatability, and reproducibility of these averaged images.

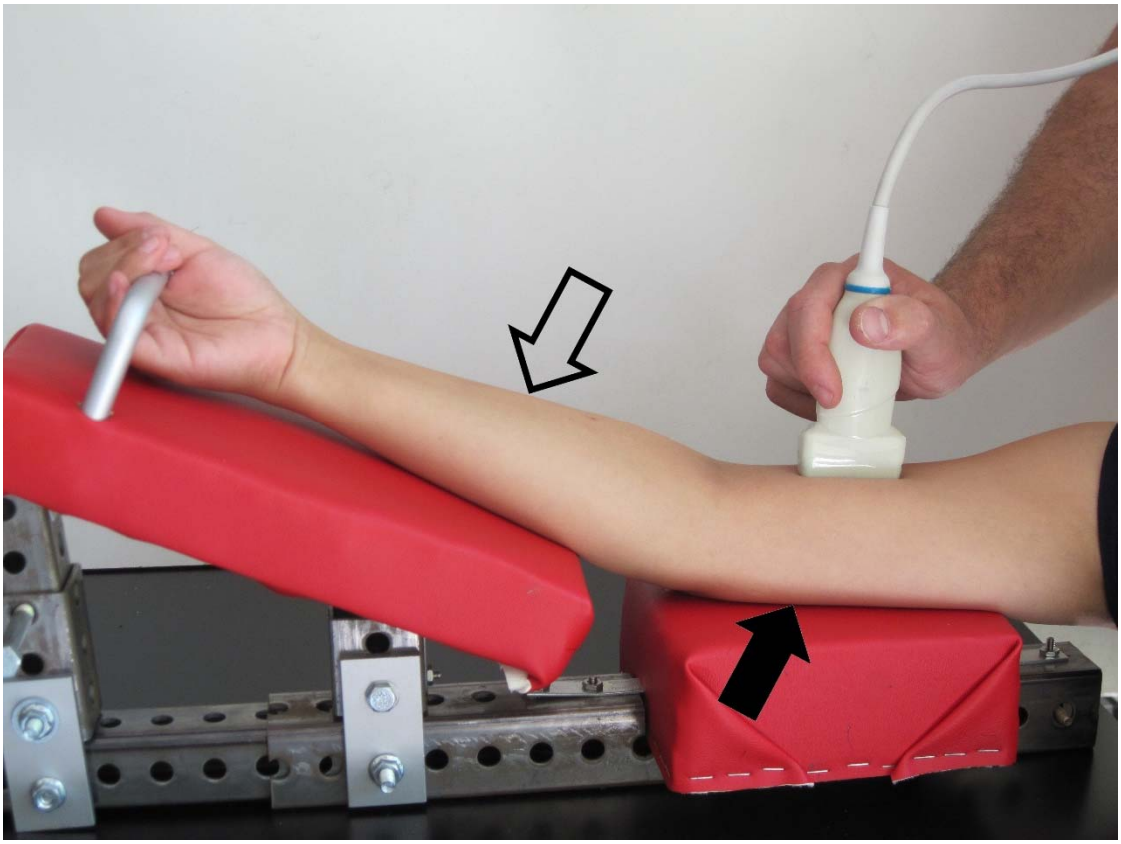

Figure 2.1: Setup for the positioning of the arm for ultrasound imaging. The upper (solid arrow) and lower (hollow arrow) arm are supported by arm pads to ensure that the biceps are relaxed and held in position. All imaging procedures were performed on the anterior portion of the upper arm as shown.

2.2.1 Establishing the Imaging Window

An adjustable armrest was used to maintain consistent positioning of the bicep during the ultrasound scans, as shown in Figure 2.1. With the arm brought out directly in front of the participant (forming a 90 degree angle to the shoulders), the posterior surface of the upper arm rested on a pad parallel to the tabletop, and the elbow was flexed to allow

the forearm to rest on a pad at 30 degrees from horizontal. The wrist was maintained in a supinated position with neutral flexion. The arm and hand were fully supported, allowing the biceps to remain in a neutral, static position with no muscle activation.

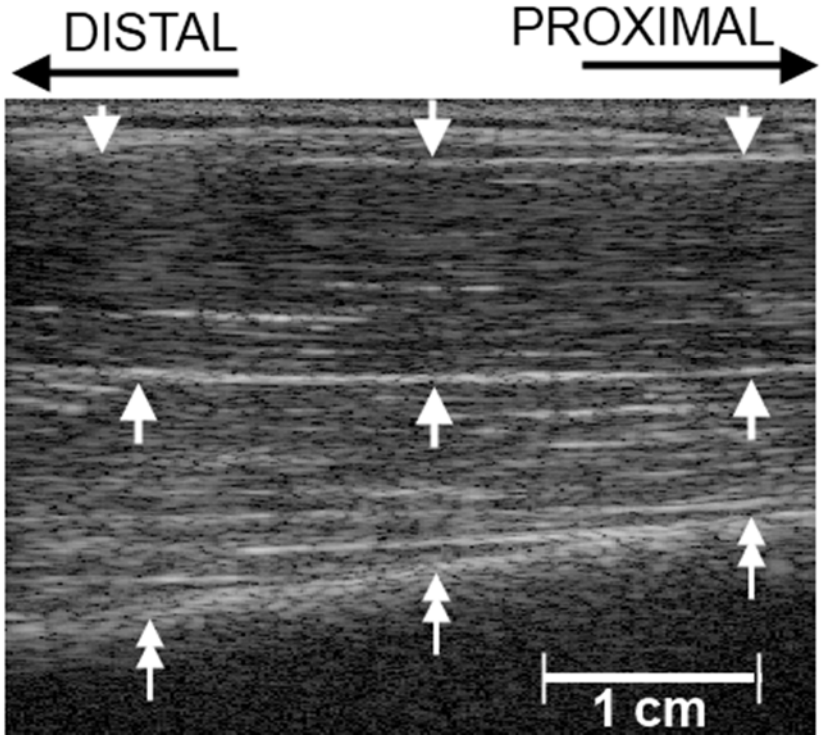

Figure 2.2: Sonogram of the upper arm with transducer oriented along the muscle fibers. The upper and lower boundaries of the biceps- brachii are denoted by the single arrows. The double arrows indicate the humerus. The area between the humerus and lower boundary of the biceps brachii is the brachialis muscle, and was not included in this study.

A transducer positioning protocol was followed to orient the transducer at the onset of each compression. During compression, the transducer motion consists only of translation along the beam axis. This constraint is ensured using a combination of external and internal structures (visible in the ultrasound B-mode image) as landmarks to establish proper transducer location and orientation. The transducer was placed on the anterior surface of the upper arm and oriented to visualize the long axis of the muscle

fibers with the distal ends of the fibers aligned with the left of the B-mode image (Figure 2.2). Using the distal biceps tendon as a starting point, the transducer was translated proximally along the midline of the muscle until the central aponeurosis was no longer visible in the B-mode image. The rotational degrees of freedom were constrained using the length, thickness, and curvature of the bone line and muscle fibers in the image as markers. The bone line of the humerus was used to indicate the alignment of the transducer with its long axis; any deviations from the axis were seen as increased curvature of the bone line. The brightness and clarity of the line indicated how well the transducer was rotated about the long axis of the humerus. A blurry or otherwise unclear bone line suggested the imaging window only partially captured the bone, so the rotation about the long axis could be corrected.

The ultrasound imaging used a Terason t3000 academic ultrasound system with a 3.81 cm (1.5 in.) wide 7.5 MHz linear array transducer (Teratech Corp. Burlington, MA, USA) set to image to a depth of 5 cm. The radiofrequency data (RF) data was recorded at 30 MHz throughout the compression. These data were represented as B-mode videos of muscle compression transverse to the fiber lengths. The RF data were recorded at approximately 31 frames per second, and the resulting frames were 1948 x 256 pixels (depth x width) in size. Each compression was 3s in duration, totaling 93 frames collected per compression.

2.2.2 Collecting Ultrasound Images

All of the ultrasound imaging procedures were performed by a researcher with over four years of experience with ultrasound systems and musculoskeletal imaging, as well as by an experienced orthopedic surgeon.

At the beginning of each freehand compression, the transducer was positioned using the

procedures described previously. The operator held the transducer and manually pressed the transducer face against the surface of the arm to compress the muscle tissue (Figure 2.1). The operator was instructed to apply a slow and steady compression for the 3s duration [10,17]. After the compression, the video data was examined to determine the frames corresponding to the onset and completion of the compression. This compression procedure was repeated 30 times with a 15s break being held between scans. This break allows the muscle to recover and ensures that the compressions were independent of each other.

Four of the nine original subjects underwent repeated freehand compressions performed by a clinician during an additional testing session. The scanning protocol was identical to that described above, except 15 compressions were recorded rather than 30.

Automated compressions were conducted using a custom developed mechanical scanner. The scanning apparatus (Figure 2.3) consisted of a transducer mounted to a one-axis linear actuator (Physik Instrumente M-229.26S, Karlsruhe/Palmbach, Germany) connected to a basic motion control system (Arcus Tech ACE-SDE, Livermore, CA, USA). The transducer was positioned according to the aforementioned standard positioning procedure before the first compression, and the positioning was maintained during subsequent scanning procedures. Thirty consecutive scans were performed with the scanning system set to compress at 2 mm/s for three seconds, and the first 5 mm of displacement were recorded.

Figure 2.3: The automated compression system provided consistent, repeatable compressions to the biceps brachii. The transducer is attached to a motor controlled by the computer. The transducer moved 5 mm.

2.2.3 Creating Strain Images

The ultrasound raw data was converted into Matlab MAT files (MathWorks, Natick, MA, USA), using a program provided by Terason [20]. A speckle tracking algorithm was used to track the motion of small groups of pixels between frames. This motion data was quantified to create a measurement of displacement for each pair of consecutive frames in a B-mode image. The algorithm employed in this study is based on well-developed techniques commonly used in the literature [20–24]. The incremental frame-to-frame strains were accumulated to calculate the total strain over the course of the compression [10]. The first 20 frames of each compression scan were analyzed to ensure the results were drawn from the same segment of the compression. Twenty was chosen as the number of frames that experienced sufficient and measurable

cumulative strain while allowing for an appropriate computation time [7]. Local strains between consecutive frames were recorded, as were the cumulative strains at each frame relative to the first frame of the 20 frame compression segment.

In the first frame of the 20 selected from of each compression, the *biceps brachii* was manually outlined and selected as the region of interest (ROI). The ROI was defined on its upper and lower boundaries by the interface of the muscle and superficial connective tissue and the interface of the *biceps brachii* and *brachialis*, respectively (Refer to Figure 2.2). The left and right boundaries were set approximately 7.5 mm from the edges of the image. Since the deformations were small over the 20 frame selection (approximately 0.065 mm per frame or 1.3 mm over the 20 frame selection), the total change in muscle depth was minimal and the same ROI mask was applied to each frame. Displacements were tracked solely within the ROI. Compression was applied along the ultrasound beam path (transverse to the muscle long axis), and the resolution is highest in this direction as well, thus, only displacements along the beam path were considered for analysis.

The mean compressive strain magnitude was calculated for each cumulative strain image. The strain image from each scan with mean strain nearest 2% was chosen for averaging. This magnitude-based selection allows for variable compression rates and magnitudes within each 20 frame scan. The cumulative strain image selected from each scan was used in the subsequent averaging procedure.

Averaged strain images for each subject were created from groups of images drawn from each set of 30 scans. Different sized groups were used to determine the minimum number of images necessary for averaging to produce improvements in strain image

quality. Thus, the images from each set were divided into groups of 1, 2, 4, and 8 images, for a total of eight groups per set of 30 images (two sets of groups of 1, 2, 4, and 8 images). The images in each group were selected at random without replacement for all groups. Within each group, the averaged strain images were defined by the equation

$$\text{Image} = \frac{\sum_{i=1}^{n} M\{i\}}{n}$$

For $n = 1, 2, 4, 8$, and $M\{i\}$ is the strain map corresponding to the `i-th' scan within each group. The strain images were aligned at the upper-left corner, then directly summed. The total summed images were then divided by the number of images included to create the average image. Thus, a total of eight averaged strain images were created from each set of scans.

2.2.4 Quantitative Comparison Metric

The final averaged images from each subject were compared visually against the strain images from the automated compressions for similarities in strain magnitude, noise levels, and strain distribution across the tissue. The mean and standard deviation of the strain magnitudes for the selected automated strain images and each of the averaged images were recorded for all subjects.

Image similarity was defined as the matrix norm of the difference in strain magnitude between any pair of strain images. The strain magnitudes in each image were normalized by the norm of the image. The resulting similarity metric, called the *norm-error*, was calculated as:

$$\text{Norm Error} = \left\| \frac{\text{Image}_1}{\|\text{Image}_1\|} - \frac{\text{Image}_2}{\|\text{Image}_2\|} \right\|$$

Where $\|x\|$ represents the matrix norm of the resulting image. Smaller values denote a higher degree of similarity between the two images. This metric was used to compare different sets of images depending on the desired outcome measure (image accuracy, repeatability, or reproducibility).

2.2.5 Accuracy, Repeatability, and Reproducibility Measurements

Strain images from single automated compressions were considered the "gold standard" of image quality. Thus, the accuracy of the averaged images was quantified through comparison of the norm-error values between these gold standard images and the averaged images from 2, 4, and 8 compressions. The norm-error between randomly selected automated strain images was considered the baseline image similarity representing the best of current clinical practice.

Repeatability was defined as the degree of similarity between the pairs of averaged images created using the same number of strain images for each subject. Given the two sets of groups of 1, 2, 4, and 8 averaged images per set of 30 scans, a total of four repeatability measurements were recorded for each subject. To illustrate, the averaged image created from one group of eight strain images was compared against the averaged image created from the second group of eight images. The resulting norm-error value was designated as the repeatability metric for that subject.

Similarly, reproducibility was quantified as the norm-error value between corresponding images from the two different ultrasound operators (one trained

researcher and one clinician). That is, for each of the four subjects scanned by the clinician, the resulting single freehand strain images and averaged images were compared against their counterparts in the original data set.

2.2.6 Statistical Analysis

All results are presented as mean ± standard deviation (SD). One-way ANOVA with Tukey HSD post-hoc test (JMP Pro 10.0, SAS, Cary, NC, USA) were performed on the repeatability measurements for 1-, 2-, 4-, and 8-image averages for all nine subjects. The same procedure was used in the comparison of averaged to automated strain images. Differences were considered statistically significant at $p < 0.05$.

2.3 Results

2.3.1 Strain Image Accuracy

Sample strain images from a single automated compression and an average of four characteristic strain images are shown in Figure 2.4. While the single automated strain image exhibits a higher degree of local variation, the strain patterns are otherwise visibly similar to the freehand averaged strain image. For a target 2% mean strain, the strain maps exhibit mean strain values of 2.37 ± 0.17% in the averaged images and 2.47 ± 0.84% in the automated images. In general, the single and averaged strain images from each subject followed this trend; comparable overall strain patterns, but with less local variability in the averaged images.

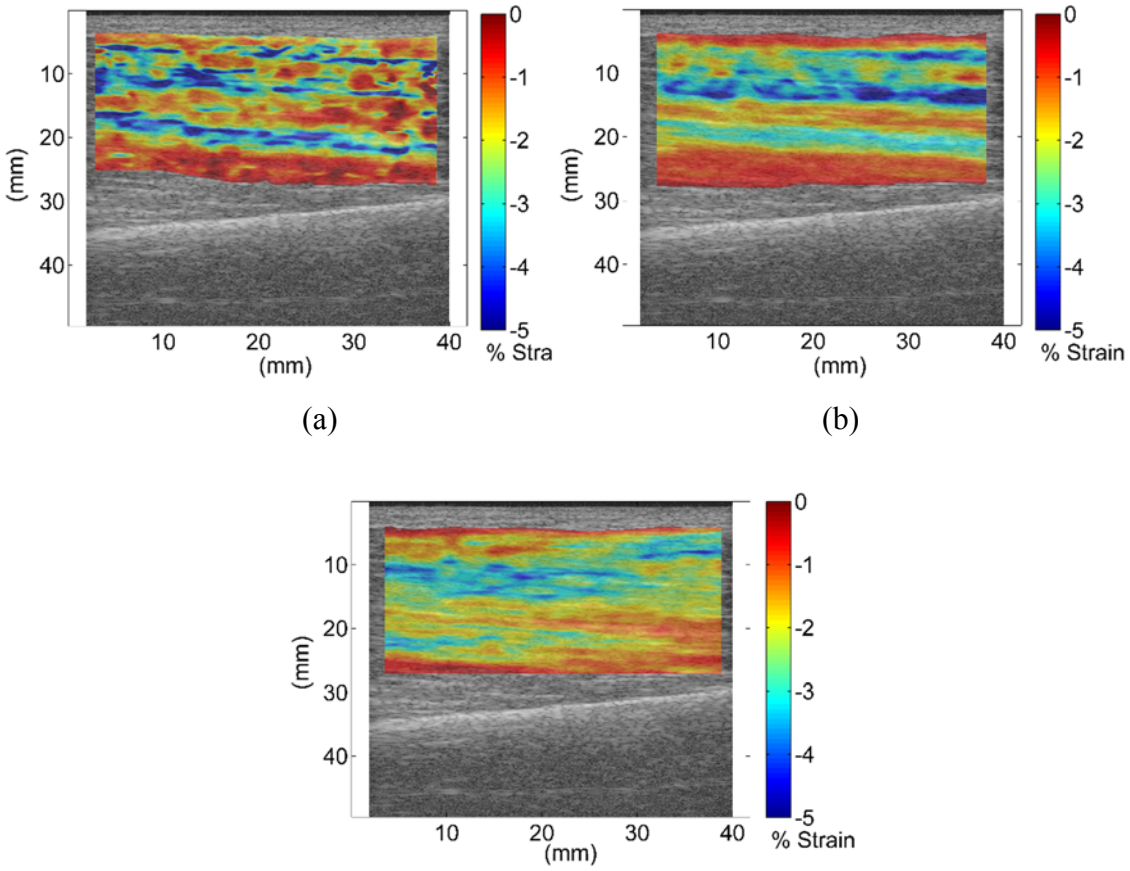

Figure 2.4: (a) A representative strain image resulting from a single automated scan of the biceps-brachii overlaid on the ultrasound image of the upper arm. The elastograms are colored to show the strain magnitude in the compression direction, with red indicating high degrees of deformation and blue indicating little to no deformation. The strain image in 4a shows considerably more local variation compared to (b) the strain image created using an average of four repeated freehand compressions, but the overall strain distribution and magnitudes are very similar. (c) Shows the strain image from an average of four repeated freehand compressions from a second operator (clinician). Again, there is a relatively high degree of qualitative similarity between the strain images.

The results from the comparison of automated strain images to averaged representative images, illustrated in Figure 2.5, show sets of strain images from automated compressions are as similar to representative images created from averaging as they are to other automated images. The mean norm-error between pairs of automated strain

images was not significantly different than the mean norm-error between automated strain images and the averaged representative images.

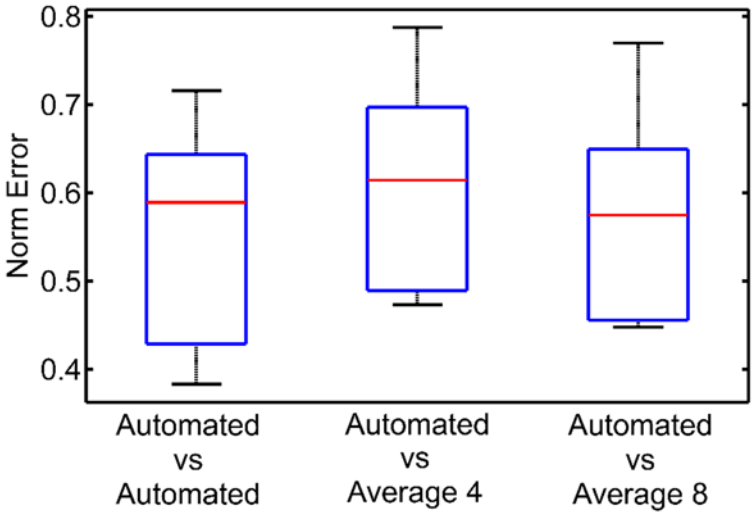

Figure 2.5: The norm-error between pairs of automated strain images, automated strain images and an average of four repeated freehand strain images, and automated strain images and an average of eight repeated freehand strain images are shown for all nine subjects. There are no significant differences ($p = 0.05$) in the mean norm-error for any of the columns. This similarity indicates that the averaged images were just as similar to the gold standard automated images as these automated images were to each other, indicating minimal data loss due to averaging.

2.3.2 Repeatability

The results of the repeatability measurements are illustrated in Figure 2.6. Smaller norm-error values indicated higher degrees of image similarity. The Single Image column in the plot refers to the similarity of pairs of single strain images resulting from automated compressions of the muscle tissue. The Average 4 and Average 8 groups showed significantly lower norm-error values ($p < 0.05$) than the Single Image, indicating increased repeatability compared to automated compressions. Mean norm-error values overall tended to decrease with increasing numbers of characteristic images included in the averaged representative image. While the mean norm-error values for

the Average 4 and Average 8 groups were not statistically different from each other, both exhibited significantly decreased error values compared to the Average 2 group.

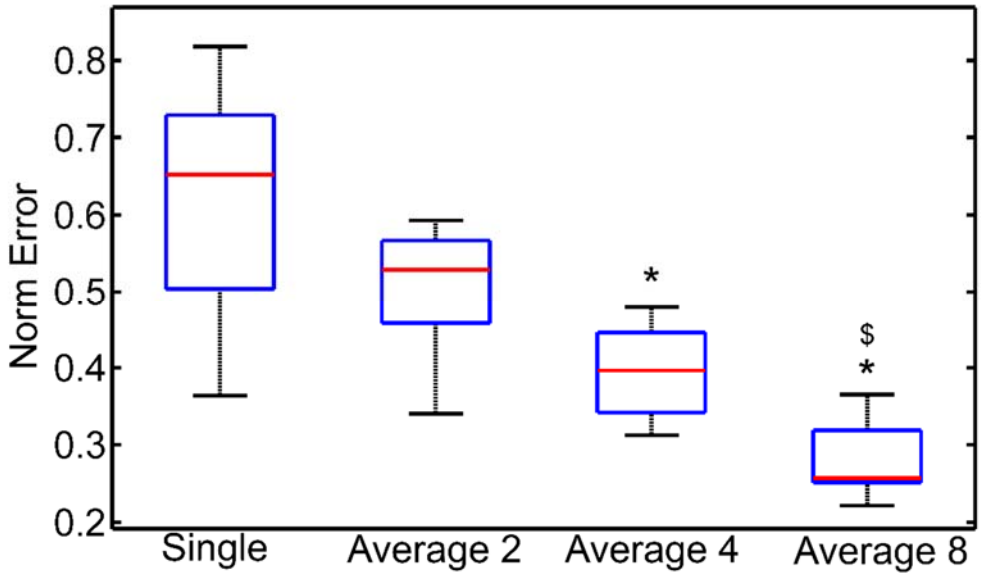

Figure 2.6: The norm-error between pairs of strain images from each type of strain image is shown for all participants. Significant differences are seen between the Single and Average 4 and Average 8 groups (*). The Average 8 also exhibited significantly different norm-error values than the Average 2 group ($), but was not different from the Average 4. All differences were considered significant at $p<0.05$.

2.3.3 Reproducibility

All three averaging groups exhibited improved inter-user reproducibility between representative images than strain images created from two single freehand compressions. However, increasing the number of images in the average from two to eight did not significantly decrease the inter-user norm error values, as can be seen in Figure 7. The decreased norm-error values of the three averaging groups compared to the single group indicate a higher degree of image similarity between users when averaging is used than when single freehand scans are used alone.

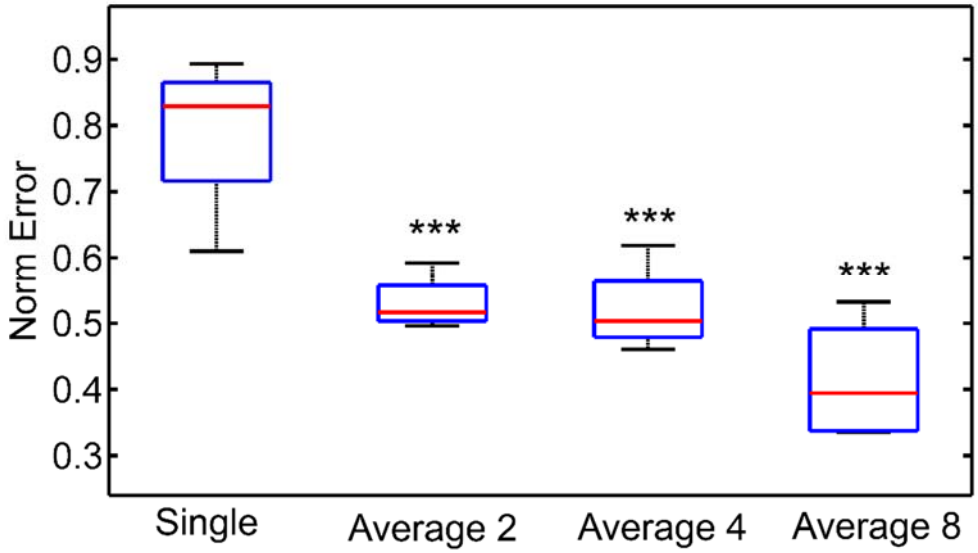

*Figure 2.7: The norm-error between pairs corresponding strain images resulting from the two operators. Averaging two or more images decreases the norm-error compared to single freehand scans, indicating an increase in reproducibility between the two operators. There were no significant decreases in norm-error with increasing the number of averaged images from two to eight. *** Significant difference from Single at $p < 0.001$.*

2.4 Discussion

Quasi-static elastography methods were used to create strain images of the *biceps brachii* of nine subjects undergoing freehand compression with the ultrasound transducer. The strain images from repeated compressions of a single subject were averaged to create the final averaged image. These averaged strain images exhibited significant improvements in intra-subject repeatability, as well as inter-operator reproducibility while remaining qualitatively and quantitatively similar to strain images created using automated compression techniques.

Unsteadiness or variability during the compression stage of quasi-static elastography has been shown to be a major source of error in the resulting strain images [18,25]. Several groups have attempted to address this issue through the use of automated or

semi-automated compression techniques that help remove the "human factor" from the process [12,17,18]. These attempts have successfully shown improvements in displacement tracking and strain image quality. The averaging procedure we describe achieves similar strain image quality using traditional freehand compression techniques. Whereas the automated systems from the aforementioned studies require additional machinery or training to improve the strain images, a simple average of repeated compressions yields qualitatively similar strain images without the extra cost of automated systems.

Not only does averaging produce similar strain images to those from automated compressions, it improves image repeatability as well. Both the Average 4 and Average 8 group evidenced increased intra-subject image similarity compared to the single automated group as well as the Average 2 group. This increase in intra-subject image similarity, or repeatability, is indicative of the decrease in noise and error in the strain images. Without the local variations prevalent in strain images from single automated scans, the averaged images are less cluttered with minimal artifacts, and the true strain patterns are more apparent.

In general, the results indicate increasing the number of images included in the average corresponded to an increase in repeatability. This increase in image similarity is most likely due to the random noise in the images being smoothed by the higher degree of averaging. Since there was no significant decrease in norm-error moving from the Average 4 to Average 8 group, the majority of the noise in the strain images is eliminated by including as little as four images in the average.

Variations in operator compression technique or transducer motion can lead to

significant noise or artifacts in the resulting strain image. For an accurate diagnosis, these sorts of inter-operator variations need to be addressed. The results of this study indicate that averaging can be used to decrease this inter-operator error by averaging strain images from as few as two repeated compressions. Similar to repeatability, the increased reproducibility is most likely due to the smoothing of the local strain magnitude fluctuations seen in strain images from single compressions. The qualitative and quantitative similarities between the single strain images and averaged strain images indicate averaging did not eliminate important image information.

Averaging strain images from repeated compressions has the additional advantage that it can be employed regardless of compression technique. Improvements in freehand compression techniques or automated compressions can be further enhanced through the addition of averaging. Although there may be extra time required for performing multiple scans, current clinical practice often selects the "best" or most representative strain image from a set of 3-5 compressions [13,14,19]. Since four strain images are all that are needed to see an improvement in the strain image consistency, there is no additional time cost associated with image acquisition using averaging.

It should be noted that for any form of tissue compression, proper transducer positioning and alignment is absolutely necessary for elastography to be effective. Changes in imaging window directly affect the speckle tracking and subsequent displacement images regardless of compression type. For scans in this study, care was taken to achieve consistent imaging windows at the onset of compression, while minimizing transducer sliding and out of plane motion during scanning to ensure accurate and representative strain images.

QSE is a highly operator-dependent technique with subjective results that make comparison between operators, patients, and experimental results difficult. As such, this technique is widely regarded as qualitative in nature, and any attempts at quantitative analysis have required specialized compression set-ups or specific imaging windows, which are not standard [13,26,27]. In this paper, we employed a norm-error measurement to attempt to quantify overall image similarity between pairs of strain images. However, this metric alone cannot be used to identify the presence or absence of key strain patterns or expected image features that may be distinctive of the specific tissue (in this case, muscle) being analyzed. Our norm-error metric does provide important information on image similarity, but must be used in conjunction with qualitative assessment of the strain images in question.

The primary limitation of this study arises from a lack of standard practice for comparing strain images. While some tissues, such as breast tissue, have been studied in some depth, and some common patterns have been linked to the presence of tumors or abnormal tissue, skeletal muscle elastography has not been explored in sufficient detail to definitively identify strain patterns corresponding to healthy tissue, let alone injured or abnormal tissue. Future work will begin to characterize common strain patterns in healthy and abnormal muscle tissue, and to develop more comprehensive image comparison techniques to quantify degree of abnormality. For example, a more complete comparison between strain images might employ image feature detection and image comparison algorithms to identify expected strain patterns within the tissue.

2.5 Conclusion

Averaging is introduced as a feasible and appropriate technique to improve ultrasound elastography of skeletal muscle. Creating an average image from a series of repeated

tissue compression cycles leads to increased intra-subject strain image repeatability and reproducibility compared to strain images resulting from automated compressions, while achieving qualitatively and quantitatively similar strain patterns. The authors recommend using strain data from 4-8 repeated compressions to create the final average image. This number of repeated compressions is similar to that already employed in clinical practice, thereby resulting in improved final strain image quality without requiring significant additional effort by the operator. Averaging may be an ideal tool to improve the final strain image quality, and ultimately diagnostic power of quasi-static elastography of muscle tissue, without the cost of additional machinery.

REFERENCES

1. Beiner JM, Jokl P, Cholewicki J, Panjabi MM. The effect of anabolic steroids and corticosteroids on healing of muscle contusion injury. Am J Sports Med . 1999;27(1):2–9.

2. Campbell SE, Adler R, Sofka CM. Ultrasound of muscle abnormalities. Ultrasound Q . 2005 Jun;21(2):87–94;153–4.

3. Martinson H, Stokes MJ. Measurement of anterior tibial muscle size using real-time ultrasound imaging. Eur J Appl Physiol. 1991;250–4.

4. Drakonaki EE, Allen GM, Wilson DJ. Ultrasound elastography for musculoskeletal applications. Br J Radiol . 2012 Nov [cited 2013 May 23];85(1019):1435–45.

5. Sarvazyan A, Hall TJ, Urban MW, Garra BS. An Overview of Elastography - An emerging branch of medical imaging. Curr Med Imaging Rev. 2012;7(4):255–82.

6. Ginat DT, Destounis S V, Barr RG, Castaneda B, Strang JG, Rubens DJ. US elastography of breast and prostate lesions. Radiographics . 2009 Nov;29(7):2007–16.

7. Hiltawsky KM, Kruger M, Ermert H, Jensen A. Freehand ultrasound elastography of breast lesions: Clinical results. Ultrasound Med Biol. 2001;27(11):1461–9.

8. Ophir J, Cespedes I, Garra B, Ponnekanti H, Huang Y, Maklad N. Elastography:

Ultrasonic imaging of tissue strain and elastic modulus in vivo. Eur J Ultrasound . 1996 Jan;3(1):49–70.

9. Friedrich-Rust M, Ong M-F, Herrmann E, Dries V, Samaras P, Zeuzem S, et al. Real-time elastography for noninvasive assessment of liver fibrosis in chronic viral hepatitis. Am J Roentgenol . 2007 Mar [cited 2012 Jul 15];188(3):758–64.

10. Doyley MM, Bamber JC, Fuechsel F, Bush NL. A freehand elastographic imaging approach for clinical breast imaging: System development and performance evaluation. Ultrasound Med Biol. 2001;27(10):1347–57.

11. De Korte C, Pasterkamp G, van der Steen A, Woutman H, Bom N. Characterization of plaque components with intravascular ultrasound elastography in human femoral and coronary arteries in vitro. Circulation . 2000 Aug 8 [cited 2012 Jul 12];102(6):617–23.

12. Varghese T, Zagzebski J, Frank G, Madsen EL. Elastographic imaging using a handheld compressor. Ultrason Imaging . 2002 Jan;24(1):25–35.

13. Drakonaki EE, Allen GM, Wilson DJ. Real-time ultrasound elastography of the normal Achilles tendon: reproducibility and pattern description. Clin Radiol . The Royal College of Radiologists; 2009 Dec [cited 2013 May 23];64(12):1196–202.

14. De Zordo T, Fink C, Feuchtner GM, Smekal V, Reindl M, Klauser AS. Real-time sonoelastography findings in healthy Achilles tendons. Am J Roentgenol . 2009 Aug;193(2):W134–8.

15. Rana M, Wakeling JM. In-vivo determination of 3D muscle architecture of human muscle using free hand ultrasound. J Biomech . Elsevier; 2011 Jul 28

[cited 2012 Jul 17];44(11):2129–35.

16. Hall TJ, Zhu Y, Spalding CS. In vivo real-time freehand palpation imaging. Ultrasound Med Biol. 2003 Mar;29(3):427–35.

17. Han L, Noble JA, Burcher M. A novel ultrasound indentation system for measuring biomechanical properties of in vivo soft tissue. Ultrasound Med Biol . 2003 Jun [cited 2012 Jul 23];29(6):813–23.

18. Kadour MJ, Noble JA. Assisted-freehand ultrasound elasticity imaging. IEEE Trans Ultrason Ferroelectr Freq Control . 2009 Jan;56(1):36–43.

19. Bhatia KSS, Rasalkar DD, Lee Y-P, Wong K-T, King AD, Yuen Y-H, et al. Real-time qualitative ultrasound elastography of miscellaneous non-nodal neck masses: applications and limitations. Ultrasound Med Biol . 2010 Oct [cited 2013 May 30];36(10):1644–52.

20. Cochran AL, Gao Y. An ultrasound elastography method for examining the anterior cruciate ligament. Nat Sci . 2013 [cited 2013 Aug 21];05(08):23–31.

21. Pesavento A, Member S, Perrey C, Krueger M, Ermert H, Member S. A time-efficient and accurate strain estimation concept for ultrasonic elastography using iterative phase zero estimation. IEEE Trans Ultrason Ferroelectr Freq Control . 1999 Jan;46(5):1057–67.

22. Chen H, Shi H, Varghese T. Improvement of elastographic displacement estimation using a two-step cross-correlation method. Ultrasound Med Biol . 2007 Jan [cited 2012 Oct 15];33(1):48–56.

23. Chen L, Housden RJ, Treece GM, Gee AH, Prager RW. A hybrid displacement estimation method for ultrasonic elasticity imaging. IEEE Trans Ultrason Ferroelectr Freq Control . IEEE; 2010;57(4):866–82.

24. Maher C, Baessler K, Glazener CM, Adams EJ, Hagen S. Surgical management of pelvic organ prolapse in women. Cochrane Database Syst Rev . 2004;(4):CD004014.

25. Chandrasekhar R, Ophir J, Krouskop T, Ophir K. Elastographic image quality vs. tissue motion in vivo. Ultrasound Med Biol . 2006 Jun [cited 2013 Aug 30];32(6):847–55.

26. Niitsu M, Michizaki A, Endo A, Takei H, Yanagisawa O. Muscle hardness measurement by using ultrasound elastography: a feasibility study. Acta radiol . 2011 Feb 1 [cited 2013 May 23];52(1):99–105.

27. Park G-Y, Kwon DR. Application of real-time sonoelastography in musculoskeletal diseases related to physical medicine and rehabilitation. Am J Phys Med Rehabil . 2011 Nov [cited 2013 Aug 21];90(11):875–86.

CHAPTER 3

EXAMINING THE FEASIBILITY OF APPLYING PRINCIPAL COMPONENT ANALYSIS TO DETECTING LOCALIZED CHANGES IN MECHANICAL PROPERTIES

3.1 Introduction

Damage to skeletal muscle tissue, such as contusions, tears, and strains, account for approximately 90% of all sports related injuries [1]. Ultrasound is recognized as a viable alternative to magnetic resonance imaging for diagnostic imaging of soft tissues, due to its portability, affordability, and real-time imaging capabilities [2,3]. Ultrasound elastography (USE), or strain-imaging, is emerging as a potential tool for monitoring and diagnosing musculoskeletal pathologies [4], however its high degree of operator-dependence has limited its widespread use.

The oldest and most prevalent USE technique is quasi-static elastography (QSE), where the ultrasound transducer is used to manually compress the tissue of interest, and record the subsequent deformation (strain) [4–6]. Visual inspection of these strain maps against a healthy baseline image can identify local regions of increased or decreased deformation levels, which correspond to regions of decreased or increased stiffness, indicating possible abnormal tissue.

In addition to this qualitative comparison, stiffness differences can be quantified by calculating the effective Young's modulus of the tissue. However, these stiffness calculations use mathematical models of the force-displacement relationship of the tissue, which usually require simplifying assumptions about the tissue properties;

including material isotropy, linear elasticity, plane strain, or plane stress [6–9]. Since muscle tissue is both nonlinear and inhomogeneous, assumptions used for modulus-based methods introduce inaccuracies to the calculated stiffness values. For QSE techniques, stiffness calculations require either the assumption of constant uniform stress, or inputs of both the applied pressure and resulting displacement. The latter necessitates additional equipment be added to the transducer to record the force data [10,11].

Further inaccuracies are introduced into QSE strain measurements by operator error. Since the compressions are usually performed freehand, the resulting displacement measurements may be affected by variations in compression magnitude and direction, as well as out-of-plane motion and transducer shaking [4,12]. These variations may cause image artifacts that can lead to misdiagnosis of tissue damage. Averaging displacement images from repeated compressions of a single subject has been shown to reduce image noise and increase intra-subject repeatability [13], but inter-subject comparisons are still affected by operator error, as well as anatomical and physiological differences between subjects.

Principal component analysis (PCA) offers a means to better account for these physiological differences and inter-operator error between subjects. PCA is a statistical technique used to identify the primary features, or principal components, common among a set of similar images. These principal components can then be combined to reconstruct an approximation of any image exhibiting the major features. Cochran and Gao (2013) showed that PCA could be used to comprehensively represent a set of simulated elastograms of the patellar tendon [14]. They also introduced a metric called the *damage-displacement,* to directly compare elastograms of injured tissue and the

healthy principal component model to locate the damaged areas and quantify their severity without the need for mathematical approximations of tissue stiffness. Therefore, with PCA and the damage-displacement technique, no additional information about applied pressure is necessary, and compressions can be performed without having to record force data.

In this study we explore the feasibility of using PCA to detect contusion injury in skeletal muscle. A finite element (FE) model of the muscle tissue subjected to both displacement- and force-controlled transverse compression was used to obtain the displacement distributions. Using the *damage-displacement* technique, we compare the healthy PCA set against individual injury FE models to explore the effects of injury size and severity on injury detectability with and without the presence of added displacement image noise.

3.2 Methods

Finite element methods were used to create a model of the *biceps brachii* muscle undergoing transverse compression, as is commonly used during quasi-static ultrasound elastography. FE models were created to represent both healthy and injured muscle tissue. A Monte-Carlo simulation was performed to select the input parameters to the healthy muscle model from a range of acceptable values. Principal component analysis (PCA) of the displacement maps generated by the FE analysis produced a representative set of normal healthy muscle variability. The injured muscle displacement maps were compared against these principal components to locate and quantify the extent of tissue damage

3.2.1 Finite Element Model

The FE analysis was performed in ABAQUS CAE (2013, Dassault Systemes, Paris, France). For the purposes of this study, the biceps muscle was approximated as a 2D rectangular structure subjected to plane stress conditions. The rectangle height was set to 15.9mm to match the average biceps depth measured in our previous studies [13]. The rectangle length and depth were based on the measurements of the Terason 12L5 linear array transducer with a 38.1mm x 10mm cross-section (Terason, Burlington, MA, USA). The 38.1mm dimension defines the width of the imaging window during ultrasonic imaging. To avoid end effects from the boundary conditions, the rectangle length was set to 152.4mm, four times the width of the imaging window (Figure 3.1).

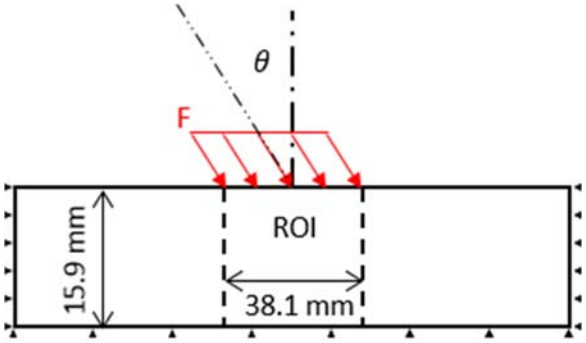

Figure 3.1: Geometry and boundary conditions of the FE model.. F represents the applied force magnitude and θ is the compression direction. θ was allowed to vary within $\pm 30°$.

The muscle substructure was approximated as alternating layers of two hyperelastic materials with separate thicknesses, corresponding to the muscle fascicles and extracellular matrix (ECM). These layers span the entire length of the muscle, with 290 and 80μm approximate thicknesses for the fascicle and ECM layers, respectively [15]. The alternating layered pattern was created by assigning the corresponding muscle fascicle and ECM material properties to individual elements based on their position in the model.

A 774 x 400 element mesh (height x length) was applied to the rectangle, resulting in a $20.54\mu m$ x $381\mu m$ element size. This element size was chosen to ensure 14 and 4 elements, respectively, per muscle fascicle and ECM layer thickness, and is approximately 4x the axial resolution of the musculoskeletal ultrasound system (Terason t3000, Terason, Burlington, MA, USA). Since the lateral strain was not as important to this study, a smaller element width was not necessary. All elements had a depth of 10mm to match the transducer thickness.

Both the muscle and ECM layers were treated as incompressible Mooney-Rivlin hyperelastic materials [15–17] with the strain energy function defined as

$$W = C_1(I_1 - 3) + C_2(I_2 - 3),$$

in which C_1 and C_2 are empirically determined material constants defined by ABAQUS, and I_1 and I_2 are the first and second principal invariants of the left Cauchy-Green tensor. The baseline material constants, C_1 and C_2, for the ECM and muscle fibers were taken from Zhang et. al. (2012). Muscle fascicles were approximated as transversely isotropic bundles of muscle fibers surrounded by ECM. New material constants for muscle fascicles were calculated using the Rule of Mixtures, assuming 90% of the fascicle volume was muscle fibers:

$$C_i = \frac{C_i^m C_i^e}{V_m C_i^e + V_e C_i^m}$$

where $i = 1, 2$, C_i is a material constant of the fascicle, C_i^m is the muscle fiber material constant, C_i^e is the ECM material constant, V_m is the volume fraction of muscle fibers, and $V_e = 1 - V_m$ is the volume fraction of ECM. The Mooney-Rivlin constants used in this study are listed in Table 3.1. The bulk modulus values, K are required as inputs in ABAQUS. To approximate tissue incompressibility, K is set to be very large relative to the corresponding C_1 and C_2 values.

Table 3.1—Healthy Material Constants

	C1 (kPa)	C2 (kPa)	K (kPa)
ECM	0.3	0.15	10
Fiber	3	1.5	100
Fascicle	2.46	1.23	100

Displacements in the lateral and axial direction were constrained to be zero on the bottom, left, and right edges of the rectangle. The top edge remained free except for a 38.1mm wide region in the center of the rectangle, which was subjected to either a constant-displacement or constant-force to model the compression by the transducer. Compressions were modeled using an applied surface traction vector to the top row of elements, with a nominal magnitude $0.0117\,N$, which induced an approximate 2% mean strain in the model.

To incorporate the effects of inter-user variability, the magnitude and direction of the compressions were allowed to vary between $0.0105\,N$ and $0.0129\,N$, representing a $\pm 10\%$ range from the baseline force magnitude. The compression direction was allowed to vary $\pm 10°$ off-axis from a pure transverse compression. The compression magnitude and angle of the applied traction vector were specified explicitly in ABAQUS.

Ultrasound imaging achieves its highest resolution in the direction of wave propagation. Therefore, most quasi-static elastography applications only measure displacements parallel to the beam-path, which is parallel to the compression. Although the FE model allows the analysis of displacement in both x and y directions, since the ideal compression in our model is orthogonal to the fiber direction, only the displacements transverse to the muscle fiber direction, i.e., u_y, were considered for PCA analysis.

3.2.2 Simulating Displacement Noise

Once displacement maps were generated, displacement error was simulated by adding Gaussian white-noise to each displacement image. The white noise was modeled as zero-mean with a standard deviation equal to 0%, 1%, 2%, or 4% of the mean overall displacement of the healthy dataset [14]. The subsequent principal component analysis and damage-displacement techniques were independently applied to each of the four resulting image sets.

3.2.3 Developing the Principal Component Model

A total of 100 FE models of healthy muscle were generated for both displacement-based and force-based compression types. Monte-Carlo simulation was used to select the material constants, compression magnitude, and compression direction from the range of acceptable values, shown in Table 2 and Table 3. The resulting FE models were analyzed and the corresponding displacement maps from each model were saved. Only the displacements from the ROI (775 x 101 nodes, 774 x 100 elements) were used in the PCA.

Table 3.2– Monte Carlo Material Constants

	$C1\ (kPa)$	$C2\ (kPa)$	$K\ (kPa)$
ECM	$0.27 - 0.33$	*0.135-0.165*	*9-11*
Fascicle	*2.214-2.706*	*1.107-1.353*	*90-110*

The principal components were calculated using the Karhunen-Lowe transform, which is a specific application of the more general single-value-decomposition methods used for computing eigenvalues [18]. 40 of the 100 original displacement maps were used to generate the PCA model, resulting in 40 Eigen-images for each compression type. The remaining 60 displacement maps were used to test the accuracy of the PCA set using the *damage-displacement* calculations described later in this paper.

Table 3.3—Monte Carlo Compression Parameters

Force-Based	Magnitude	Direction
	0.0117 N	$-10° - 10°$

3.2.4 Injury Model

Contusion injuries were modeled by independently changing the material properties and diameter of localized circular regions. Each region was located in the center of the ROI.

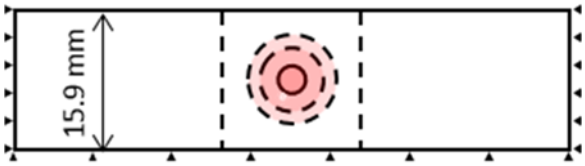

Figure 3.2: Geometry of the injured model. A circular injury area was located at the exact center of the ROI with various sizes: 2mm, 4mm, 10mm, and 20mm diameter regions.

The injured area was also modeled as an incompressible Mooney-Rivlin material. Injury severity was modeled as an increase or decrease in the material constants relative to the muscle fascicle values. These injured material properties were defined as -50%, -25%, -10%, -5% decreases in material constant values, as well as 5%, 10%, 25%, 50%, and 100% increases in magnitude to represent areas of decreased and increased stiffness, respectively. The bulk modulus for the injured areas was held constant at $K = 100$, as it is sufficiently large to represent tissue incompressibility. A total of 50 injury models were created for each severity, and the injury size was maintained at $8\ mm$ diameter.

An additional 400 injury models were generated with variable contusion sizes. Four diameters were used: $2\ mm, 4\ mm, 10\ mm,$ and $20\ mm$, each with 50 simulations. These variable-size injuries were specified to have either a 50% decrease or 100% increase in material constants relative to the muscle fascicles. These injury severity levels were selected to represent a significant and detectable injury according to the

results of the variable-severity study.

3.2.5 Damage-Displacement

The damage-displacement, defined as localized difference between the displacement maps from individual models and the representative PCA sets, was computed as described by Cochran, et. al. 2014. Briefly, the displacement maps from each individual model were approximated with linear combinations of all of the Eigen-images from the healthy muscle. Subtraction of the resulting approximated image from the single displacement image identifies the local regions within that displacement map that cannot be represented by the PCA set. The resulting *damage-displacement* image, w, can be represented by

$$w = (u - \bar{u}) - \sum_{i=1}^{L} \langle p_i, u - \bar{u} \rangle p_i,$$

where u is the test image, $\bar{u}$ is the mean of the test image, p_i is the 'i-th' principal component, and $\langle \cdot, \cdot \rangle$ represents the standard Euclidian dot product. The resulting *damage-displacement* maps were normalized by the original injured displacements to quantify the Relative Magnitude (RM) of the damage displacement according to the equation:

$$RM = \frac{|w|}{|u|}$$

The d*amage-displacement* maps and corresponding RM were calculated using displacement maps from each of the 30 healthy muscle models to test the accuracy of the PCA model. The resulting values provided a measure of relative error in the PCA model, since the theoretical value of w for a healthy muscle should be zero [14].

Similarly, the d*amage-displacement*s and RM of each of the injury models were calculated to identify muscle contusions. Injuries were defined as mean RM values

greater than the mean plus two standard deviations of the healthy values. Injury severity was graded based upon the RM magnitude.

3.2.6 Strain Calculations and Contrast-to-Noise

We measured the contrast between the healthy and injured tissue regions from images of *damage-strain*, which is defined as the partial derivative of the *damage-displacement* with respect to the axial direction [14]. The lateral direction *damage-displacement* maps were linearly interpolated onto into $80\mu m$ segments, but the axial direction remained at $20.54\mu m$ spacing. Strains were calculated with a 60-by-10 sample (1.2mm-by-0.8mm) kernel, and subsequently linearly interpolated back onto the original $20.54\mu m$ x $381\mu m$ grid. The contrast-to-noise ratio (CNR) between the healthy and injured regions was calculated as:

$$CNR = \frac{2\left(\mu_{injured} - \mu_{healthy}\right)^2}{\sigma_{injured}^2 + \sigma_{healthy}^2}$$

where μ and σ represent the mean and standard deviation of the *damage strain*, respectively, measured in the injured and healthy regions. The CNR was calculated for all 12 injuries from each compression type.

3.2.7 Statistics

All comparisons were made using one-way analysis of variance (ANOVA). Tukey HSD post-hoc analysis was performed to with the results of the ANOVA to determine specific group-to-group differences. All differences were considered statistically significant at $P < 0.05$.

3.3 Results

3.3.1 *Healthy Displacement Images*

Figure 3.3 shows sample displacement image of the healthy FE models under compression for 0%, 1%, 2% and 4% image noise. The displacement magnitudes correspond to deformation in the y-direction. The displacement patterns were significantly affected by compression angle, as seen by the "slanted" gradient in Figure 3.3.

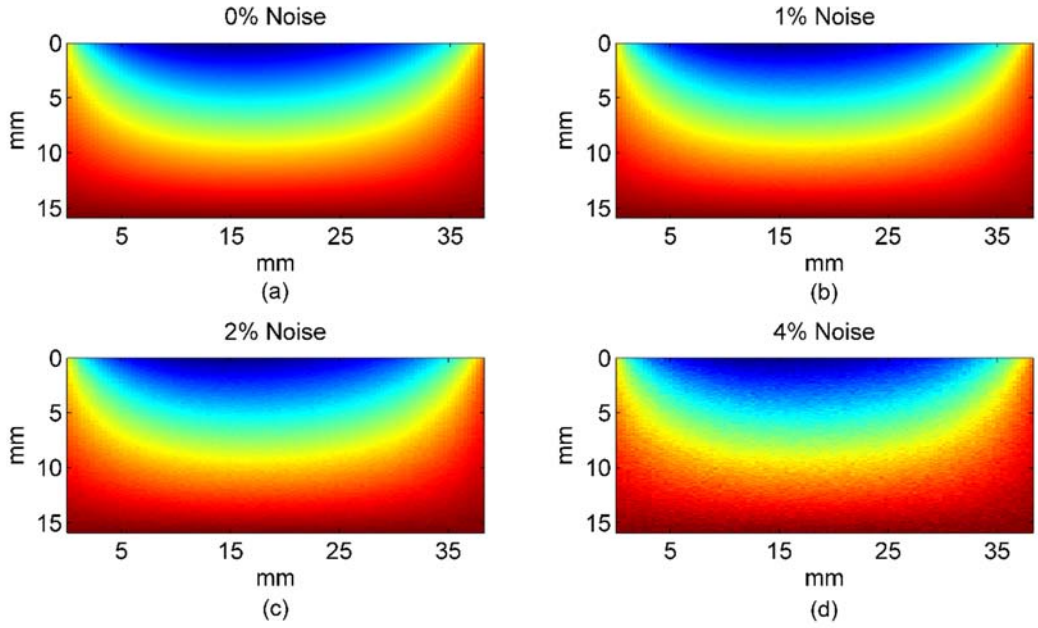

Figure 3.3: Sample FE displacement images of healthy muscle undergoing transverse compression for (a) 0%, (b) 1%, (c) 2%, and (d) 4% added image noise.. All displacement values are measured in millimeters.

3.3.2 *Injury Severity*

Injury areas with increased stiffness relative to the surrounding tissue exhibited higher Relative Magnitude values than softer injury areas, regardless of displacement noise. However, within the positive and negative injury groups, respectively, injury severity had no effect on the Relative Magnitudes. Figure 3.4 shows the effect of injury severity and noise level on the Relative Magnitude measurements. For both types of

injury, statistically significant increases in Relative Magnitudes were seen for differences as small as 5% for all noise levels. Increasing noise levels significantly increased the Relative Magnitude values at each injury level by a near-constant value, resulting in a net upward shift of Relative Magnitudes ($p < 0.05$).

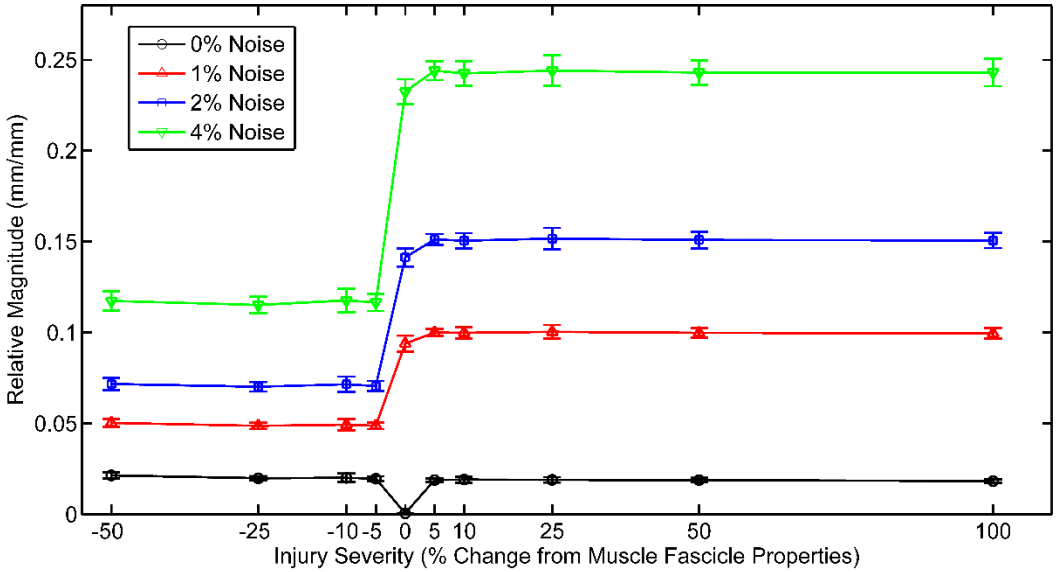

Figure 3.4: Relative Magnitude values as a function of injury severity and added image noise. No statistical differences were seen between the positive injury groups. Only the -50% severity group exhibited significantly larger Relative Magnitude values compared to the other negative severities. All

Figure 3.5 shows the CNR as a function of injury severity for all four noise levels. At zero noise, the CNR exhibited a negative correlation to increasing stiffness ($p < 0.001$). Among the decreased stiffness groups, only the -10% severity showed statistically different CNR values, while the increased stiffness groups were not statistically significant from each other, but were all significantly lower than the decreased stiffness CNR values ($p < 0.05$). The addition of noise to the displacement images greatly reduced the CNR for all injury levels. These low CNR values can be seen in Figure 3.6, which shows a set of sample Relative Strain maps for the -50% and 100% injury groups

at all four injury levels.

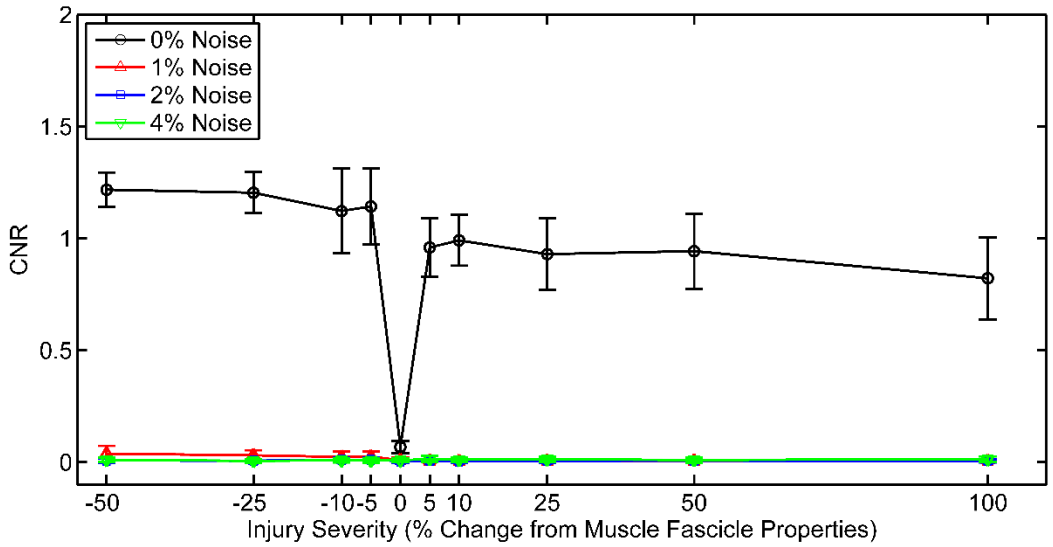

Figure 3.5: Contrast-to-noise (CNR) ratio as a function of injury severity and noise level. CNR was negatively correlated with increases in stiffness. The addition of noise significantly reduced the CNR values for all injury severities.

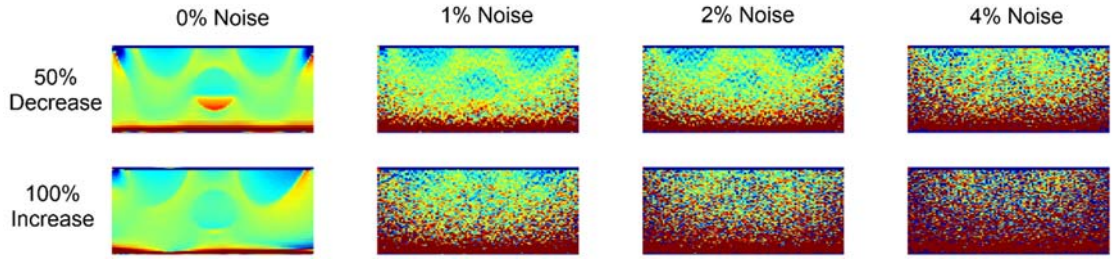

Figure 3.6: Sample Relative Strain images for -50% and 100% injury severity groups at each of the four noise levels. Darker areas correspond to larger Relative Strain values, indicating potentially damaged areas. The circular injured areas become less and less visible with increasing noise levels, which result in the decreased CNR seen in Figure 3.5.

3.3.3 Injury Size

At zero added displacement noise, increasing the injury diameter resulted in statistically significant increases in Relative Magnitude for both positive and negative changes in

injury stiffness, as seen in Figure 3.7. There were no statistical differences in Relative Magnitude at any injury size between the -50% and 100% injury levels. Higher noise levels resulted in consistently higher Relative Magnitude values for all injury sizes, similar to those illustrated in Figure 3.4.

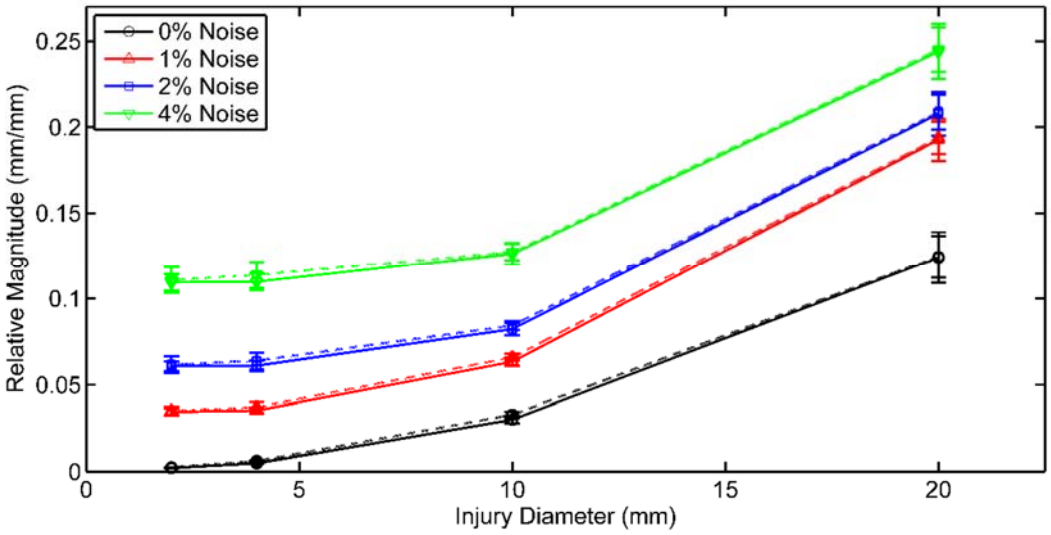

Figure 3.7: Relative Magnitudes of as a function of injury diameter. Solid lines (-) represent regions of increased stiffness while dotted lines (--) show softer injuries. There were no significant differences between Relative Magnitudes of hard and soft injuries for any diameter.

Although the $20\ mm$ diameter injuries exhibited the largest Relative Magnitude values, the injured areas exhibited significantly lower CNR values compared to the $10\ mm$ injury with significance $p < 0.001$ (Figure 3.8). This decreased CNR can be attributed to the larger size of the injury affected region, as illustrated in Figure 3.9. Compared to the smaller injuries, the $20\ mm$ diameter injuries affect a much larger portion of the ROI, resulting in a higher background signal which obscures the injured area. The CNR

values for the softer injuries were higher for all four injury sizes with significance $p < 0.001$.

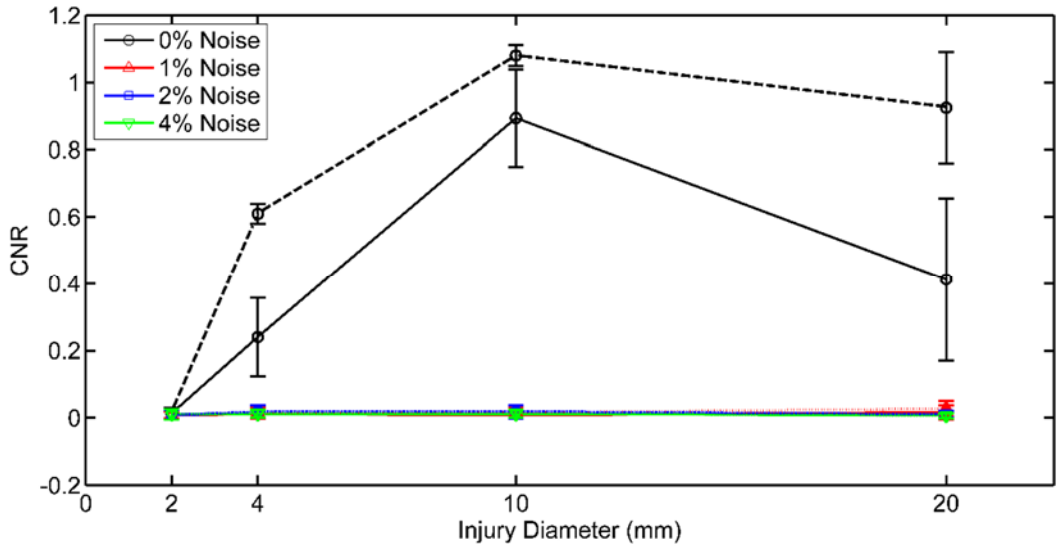

Figure 3.8: CNR as a function of injury diameter. 10 mm diameter injuries exhibited the highest CNR for both hard (solid lines) and soft (dotted lines) regions. The addition of image noise once again drastically reduced the CNR for all injury sizes, regardless of material properties.

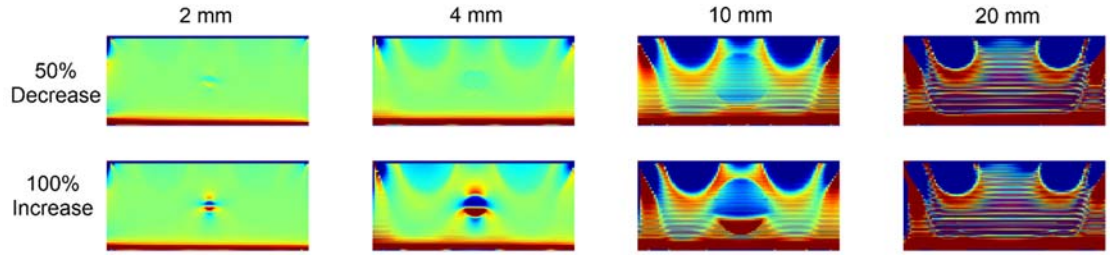

Figure 3.9: Sample Relative Strain images for -50% and 100% injury severity groups at each of the injury sizes. The circular damaged regions are most readily visible in the 4mm and 10mm diameter areas for both sets of material properties.

3.4 Discussion

The goal of this study was to determine the effects of localized changes in mechanical

properties on the resulting displacement images in a FE model of skeletal muscle. PCA and *damage-displacement* were used to quantify and visualize the changes to displacement maps for modeled injuries of various size and severity. Muscle injuries, such as contusions, damage the tissue structure, thereby affecting the mechanical behavior of the tissue in the injured areas. The FE model was designed to approximate the basic geometry and loading conditions of the *biceps brachii* during standard QSE compressions with and without a simulated injury. By varying the material properties and diameter of the simulated circular injury, we explored the effects of injury severity and size on the ability of PCA to quantify and visually locate damaged areas, with and without the addition of image noise.

The results of the zero-noise analyses show that there is a trade-off between Relative Magnitude and CNR for soft and hard damage regions. However, within the major categories of "hard" and "soft" material properties, the magnitude of the difference between the damaged region properties and those of the surrounding tissue have little to no effect on the resulting PCA error.

While areas of increased stiffness result in higher Relative Magnitudes compared to decreased stiffness regions, they are not as readily identified in the final Relative Strain images compared to softer regions. The decrease in CNR for stiffer regions may be partially caused by the higher overall Relative Magnitude values. The localized stiff regions divert much of the deformation to the surrounding material, causing a larger area of affected displacements which cannot be fully represented by the principal components. The result of this dispersion is a stronger background signal, as seen in the 100% injury plots of Figures 3.4 and 3.9, compared to the -50% regions. Conversely, with the softer regions, the surrounding tissue deforms much the same as

with healthy tissue. Only the region of decreased stiffness and a small area around it undergo increased displacements, resulting in a weaker background signal and stronger CNR. However, visual inspection of the strain images clearly show the circular injury regions for both hard and soft tissue regions.

Differences in mechanical properties are most readily seen for $10\,mm$ diameter damaged regions, as indicated by Figure 3.8. The $10\,mm$ diameter corresponds to near 25% of the width of the ROI, and 63% of the muscle depth. Injuries of this size and smaller were far enough from the edges of the image to avoid interference with the boundary effects caused by the compression and fixed surface. Although the $20\,mm$ injury exhibited the highest degree of disagreement from the healthy principal components, as indicated by the large Relative Magnitude values, it was too large to be clearly distinguishable from the surrounding material. The resulting strain patterns blended with the edge effects to partially obscure the injured boundaries.

Surprisingly, image noise was a significant factor in the accuracy of PCA representation of displacement patterns for both the healthy and damaged models. These results are in stark contrast with the work published by Cochran, et. al. 2013, who showed that PCA could readily detect damage regions in a simulated patellar tendon regardless of noise levels. However two major differences between these two studies may have affected the noise effects: (1) Loading conditions, namely axial tension rather than transverse compression, and (2) modeling ligaments rather than muscle, where ligaments are generally a stiffer tissue. For example, our results show that the variable compression direction greatly affects the displacement patterns. For ligaments subjected to axial tension, the loading direction remains constant, but the imaging window may change, resulting in less substantial changes to the variation in the displacement patterns.

Examination of the PCA technique applied to the healthy images in this study shows that the cross-correlation matrix representing the healthy dataset has only three significant singular values, corresponding to the three largest eigenvalues. The next largest eigenvalue is sufficiently small that even the smallest amount of noise (we tested as low as 0.1%) dominated its contribution. Even the addition of up to 30 additional images in the healthy dataset was not able to strengthen these eigenvalues. Once again, these results are in stark contrast to the patellar tendon study, in which upwards of 8-10 significant principal components were seen. These results suggest that the normal variation in healthy muscle displacement maps is too large to exhibit sufficient image features to overcome the noise effects, even though the noise does not drastically affect the appearance of the displacement patterns (Figure 3.3).

Since ultrasound images and their resulting elastograms are inherently noisy, the reasons for this noise dominance needs to be more fully understood. Future work will examine the effects of different baseline displacement patterns on the resulting principal components. It is possible that this model used too great a range of variation in compression parameters to be encompassed by the PCA. Alternately, axial stretching, like that employed by Cochran et. al. can be applied in lieu of the compressions. This loading mechanism would be similar to a muscle contraction, and may provide a stronger set of eigenvalues. Additional work would explore alternative PCA algorithms that may prove more robust to the presence of noise in the input images.

3.5 Conclusion

PCA combined with the *damage-displacement* metric is shown to be a feasible tool for detecting and quantifying localized changes in mechanical properties using displacement images output by a finite element model of muscle tissue under

compression. It can identify changes in mechanical properties as low as $\pm 5\%$ relative to the surrounding tissue, as well as injuries as small 5% of the image depth. However, this technique is highly sensitive to displacement noise, and future work is needed to mitigate these noise effects before PCA can be used with the inherently noisy QSE generated displacement images.

REFERENCES

1. Beiner JM, Jokl P, Cholewicki J, Panjabi MM. The effect of anabolic steroids and corticosteroids on healing of muscle contusion injury. Am J Sports Med. 1999;27(1):2–9.

2. Campbell SE, Adler R, Sofka CM. Ultrasound of muscle abnormalities. Ultrasound Q. 2005;21(2):87–94; quiz 150, 153–4.

3. Martinson H, Stokes MJ. Measurement of anterior tibial muscle size using real-time ultrasound imaging. Eur J Appl Physiol. 1991;250–4.

4. Drakonaki EE, Allen GM, Wilson DJ. Ultrasound elastography for musculoskeletal applications. Br J Radiol. 2012 Nov;85(1019):1435–45.

5. Ophir J, Cespedes I, Ponnekanti Y, Yadzi Y, Li X. Elastography: A quantitative method for imaging the elasticity of biological tissues. Ultrason Imaging. 1991;134:111–34.

6. Sarvazyan A, Hall TJ, Urban MW, Garra BS. An Overview of Elastography - An emerging branch of medical imaging. Curr Med Imaging Rev. 2012;7(4):255–82.

7. Doyley MM, Srinivasan S, Pendergrass SA, Wu Z, Ophir J. Comparative evaluation of strain-based and model-based modulus elastography. Ultrasound Med Biol. 2005;31(6):787–802.

8. Shore SW, Barbone PE, Morgan EF. NIH Public Access. 2012;133(6):1–34.

9. Gokhale NH, Barbone PE, Oberai A a. Solution of the nonlinear elasticity imaging inverse problem: the compressible case. Inverse Probl. 2008 Aug 1;24(4):045010.

10. Han L, Noble JA, Burcher M. A novel ultrasound indentation system for measuring biomechanical properties of in vivo soft tissue. Ultrasound Med Biol. 2003 Jun;29(6):813–23.

11. Niitsu M, Michizaki A, Endo A, Takei H, Yanagisawa O. Muscle hardness measurement by using ultrasound elastography: a feasibility study. Acta radiol. 2011 Feb 1;52(1):99–105.

12. Kadour MJ, Noble JA. Assisted-freehand ultrasound elasticity imaging. IEEE Trans Ultrason Ferroelectr Freq Control. 2009 Jan;56(1):36–43.

13. Leineweber MJ, Westborn J, Cochran A, Choi J, Gao Y. Averaging Improves Strain Images of the Biceps-Brachii Using Quasi-Static Ultrasound Elastography. Br J Radiol. 0(0):20130624.

14. Cochran AL, Gao Y. A numerical method to detect soft tissue injuries from tissue displacements. Inverse Probl Sci Eng. 2013;0(0):1–23.

15. Zhang C, Gao Y. Finite element analysis of mechanics of lateral transmission of force in single muscle fiber. J Biomech. 2012/06/12 ed. 2012;45(11):2001–6.

16. Teran J, Blemker SS, Hing VNT, Fedkiw R. Finite Volume Methods for the Simulation of Skeletal Muscle. Eurographics/SIGGRAPH Symposium on Computer Animation. 2003. p. 68–75.

17. Sharafi B, Blemker SS. A mathematical model of force transmission from intrafascicularly terminating muscle fibers. J Biomech. Elsevier; 2011 Jul 28;44(11):2031–9.

18. Shlens J. A Tutorial on Principal Component Analysis. CoRR. 2014;abs1404.11.

CHAPTER 4

MONITORING SKELETAL MUSCLE RECOVERY IN A RAT INJURY MODEL USING ULTRASOUND IMAGING

4.1 Introduction

Skeletal muscle injury accounts for up to 55% of all sports-related injuries, and 90% of these injuries are either muscle strains or contusions [1–3]. Both strain and contusion injuries are considered to be *shearing injuries,* and are characterized by disruption of the muscle fibers, connective tissue, and nearby capillaries [3]. Although muscle is capable of healing after injury, incomplete functional recovery often occurs, possibly as a result of the presence of scar-tissue, fibrosis, and fatty infiltration post-injury [2,4]. Better understanding of the healing process and tissue morphologies during muscle regeneration can help guide treatment options and promote full functional recovery.

Imaging modalities, such as magnetic resonance (MRI) and ultrasound are used to non-invasively determine valuable structural and physiological information about muscle tissue [5,6]. Ultrasound imaging, in particular, is recognized as a useful tool for soft tissue imaging and a viable alternative to MRI for some musculoskeletal applications due to its affordability, portability and real-time imaging capabilities [7,8]. These three attributes, in particular, make ultrasound ideal for use as an early-stage diagnostic tool, as well as for monitoring of tissue recover after injury.

Skeletal muscle has transversely isotropic structure, and therefore, standard B-mode images of healthy skeletal muscle appear as either bright striations or dots, depending on whether the transducer was oriented parallel or transverse, respectively, to the muscle fibers. Muscle fibers are themselves relatively hyperechoic, with the brighter areas corresponding to the connective tissue between fiber bundles [9,10]. Tissue

damage is usually assessed by qualitative or semi-quantitative visual analysis of any disruptions to these patterns, including localized acute changes, as well as increases or decreases in the overall echointensity of the image [9,11,12]. Scales, such as those developed by Heckmatt [13] and Campbell [11], have been used to quantify tissue abnormality using ultrasound images. Numerical scores are assigned to each imaged based on the clinician's interpretation of the image, using well-defined indicators of damage, such as missing or incomplete structures, or increases in echointensity.

Ultrasound is ideal for monitoring tissue health over multiple time points. Of particular interest is the application of ultrasound to evaluating muscle recovery after an injury, especially in regards prescribing treatment options. Although there has been extensive work into evaluating injuries immediately, as well as at sporadic time-points after injury, no studies have specifically used ultrasound imaging to monitor skeletal muscle regeneration.

In this study we combine muscle functional testing and ultrasound imaging to evaluate muscle health before and after contusion injury. We develop an Injury Score to grade the severity of damage seen from the ultrasound images at each time-point, using muscle strength as an indicator of muscle health. The goal of this study is to determine the sensitivity of ultrasound images to injury severity, namely how long after injury ultrasound imaging is able to detect damage to skeletal muscle.

4.2 Methods

Experiments were performed on the right gastrocnemius muscle of 8-week old (n=8) male Wistar rats. All test procedures were approved by the Cornell University IACUC. Ultrasound images of the gastrocnemius undergoing transverse compression were

recorded for use with USE, and in-situ torque test were performed to determine contractile function of the muscle. Isometric contraction strength of the gastrocnemius was used as an indicator of muscle health throughout the study. Both ultrasound imaging and functional muscle testing were performed before injury, as well as 1, 3, 7, and 14 days post-injury. The ratio of muscle strength relative to pre-injury strength at each time was used to quantify the amount of damage present. Ultrasound imaging and PCA analysis performed at the same time points were used to locate and determine the degree of muscle injury, which were compared to the results by functional test.

4.2.1 Functional Testing Procedures

The isometric contraction strength of the gastrocnemius muscle was measured by in-situ torque test as described in our previous study [14]. Briefly, the rats were first anaesthetized with isoflurane and placed in a supine position onto a custom testing platform. The foot was secured onto a footplate and positioned 90° to the tibia. The knee was also bent to 90° and a Kirschner wire was driven through the proximal tibia to stabilize the joint. A schematic of the test set-up is shown in Figure 4.1.

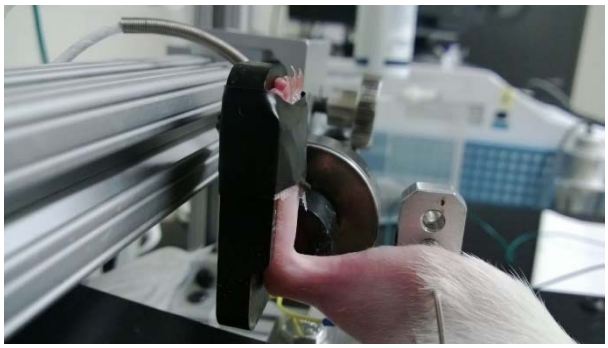

Figure 4.1: The set-up of the right-hindlimb in the torque-testing apparatus is shown. With the animal placed in a supine position, the foot is secured in the footplate by tape (left) and the ankle joint is set to 90°. *The Kirschener wire is driven through the proximal tibia, just below the knee (right-side of the image) to hold the leg in place during testing. The stimulation needles are not shown.*

Monopolar needle electrodes were used to stimulate the gastrocnemius muscle to induce contraction. Stimulation was achieved using 1ms pulses at 100 Hz, with 15 mA of constant current 20 V signal for 2s. These stimulation values were chosen from a previous study [14], where they were shown to produce near-maximal tetanic contraction.

As with the ultrasound imaging, torque testing was performed prior to and immediately after contusion injury, as well as 3, 7, and 14 days post-injury. The torque values were all normalized against the pre-injury levels to calculate the percent-of-healthy-baseline muscle strength.

4.2.2 Contusion Injury

Contusion injury was induced by the method we used in the previous study [14,15]. Briefly, the rats were sedated and placed in the prone position. The right hind-limb was manually secured to a half-cylindrical fixture with the ankle at neutral flexion and the knee extended. The fixture ensured that the gastrocnemius was oriented towards the oncoming indenter. A 500 g mass was dropped from 33cm onto a semi-spherical

indenter that was in contact with the skin over the gastrocnemius to induce injury. After injury, rats were allowed unlimited activity.

4.2.3 Ultrasound Imaging

Ultrasound images were recorded using the Vevo 770® High Resolution Imaging System (FUJIFILM Visualsonics, Toronto, ON, Canada) coupled with the RMV 704 scanhead. The ultrasound center frequency was set to 40 MHz with 30 frames per second data acquisition rate, corresponding to a 10mm x 10mm imaging window.

The rats were placed prone on a flat surface with the right-hind-limb extended behind the animal, and the fur was removed from the posterior surface of the gastrocnemius. Ultrasound gel placed between the scanhead and the skin. The scanhead was oriented to orthogonal to the tibia such that the muscle fibers were clearly seen in the ultrasound image. The distal insertion and tibia were used as internal reference points for establishing the imaging window. Figure 4.2 shows a schematic of the positioning of the transducer on the posterior gastrocnemius.

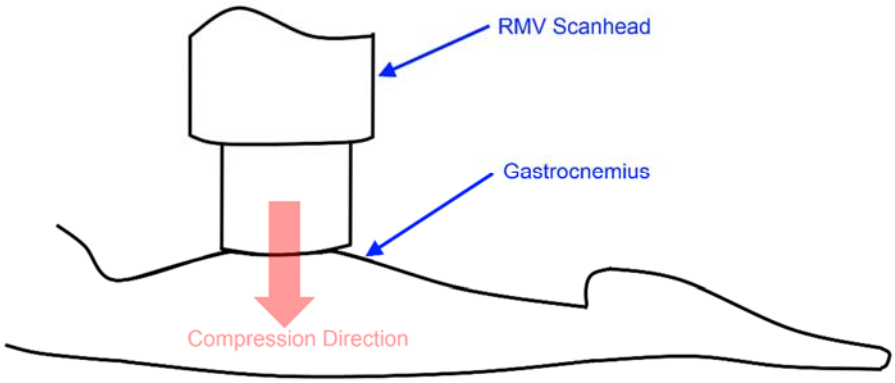

Figure 4.2: The rat hindlimb in the prone position is shown with the ultrasound RMV 704 scanhead positioned against the posterior surface of the gastrocnemius muscle. During the imaging procedures, the scanhead was pressed against the surface of the muscle to cause tissue compression against the tibia near the anterior surface of the leg.

4.2.2 Image Processing

Ultrasound data was recorded throughout the compression, and the B-mode images were saved as AVI videos. The image data was extracted for each frame, resulting in sets of 40 grayscale images of size 490x430 pixels. Each image was processed with a medial filter employing a 3x3 pixel kernel to smooth the salt-and-pepper noise overlaid on the images during the AVI conversion. Single frames from each video were selected for visual inspection of injury severity.

4.2.5 Grading Injury Severity

Tissue damage was graded using a custom numerical scale developed for analyzing contusion injury. Each ultrasound B-mode image was assigned a number from 0-5 corresponding to injury severity, with 0 indicating no visible tissue damage and 5 indicating very severe damage. The scale was based on visual indications of injury, and the specific criteria for each level are described in Table 1.

The injury grading was performed by a seasoned expert ultrasound imaging with over 60 years of experience. Prior to image analysis, the user was subjected to a training program to create familiarity with the grading scale. Training was performed with a set of 12 images, corresponding to two images from each injury level. During the grading procedure, images were presented in random order, and the grader was blinded to both the animal number and days after injury for each image. A total of 360 images (76 per day) were subjected to scoring.

Table 1: Injury Severity Scale

Level	Description
0	• Strong and obvious muscle striations • Separated and distinguishable gastrocnemius and soleus • Near uniform soleus thickness with strong bone-line
1	• Weakening of muscle striations. Increase in speckling • Muscle structure is still visible and uninterrupted with continuous boundaries • No significant swelling or increase in muscle thickness
2	• Muscle structure is compromised with unclear or broken boundaries • Bone line is still mostly visible • No significant swelling or increase in muscle thickness.
3	• Bone-line is incomplete or missing • Increased separation between surface and soleus, indicating muscle swelling • Incomplete muscle boundaries with localized anechoic areas that do not penetrate more than 25% into the muscle belly
4	• Localized anechoic regions encompassing 30-60% of the muscle belly. • Swelling and 25-50% increase in muscle thickness from healthy values • Slightly convex boundary between gastrocnemius and soleus
5	• Muscle thickness increase >50% of healthy values • Anechoic regions encompassing >60% of the muscle belly • Pronounced curvature to gastrocnemius-soleus boundary

4.2.6 Statistics

Differences in muscle torque and severity values were determined using a one-way analysis-of-variance (ANOVA) with repeated measures. The values were grouped by day, with inter-rat variation treated as a random effect for both torque and image analysis studies. Tukey-HSD post-hoc least squared means testing was performed to identify differences between specific days. Differences were considered statistically significant at $p < 0.05$. All statistical analyses were made using JMP Pro 10.0 (SAS, Cary, NC, USA).

4.3 Results

4.3.1 Muscle Strength and Contusion Injury

The drop-tower created significant contusion injury in all 8 rats, indicated by decreases in muscle strength (Figure 4.3), as well as acute swelling of the gastrocnemius in several of the rats, along with visible hematoma. Muscle contraction strength decreased to approximately 60% of healthy values immediately post-injury. Although there are not

statistical differences between 1, 3, and 7 days after injury, there is an upward trend in muscle strength, resulting in near-baseline values by Day 14.

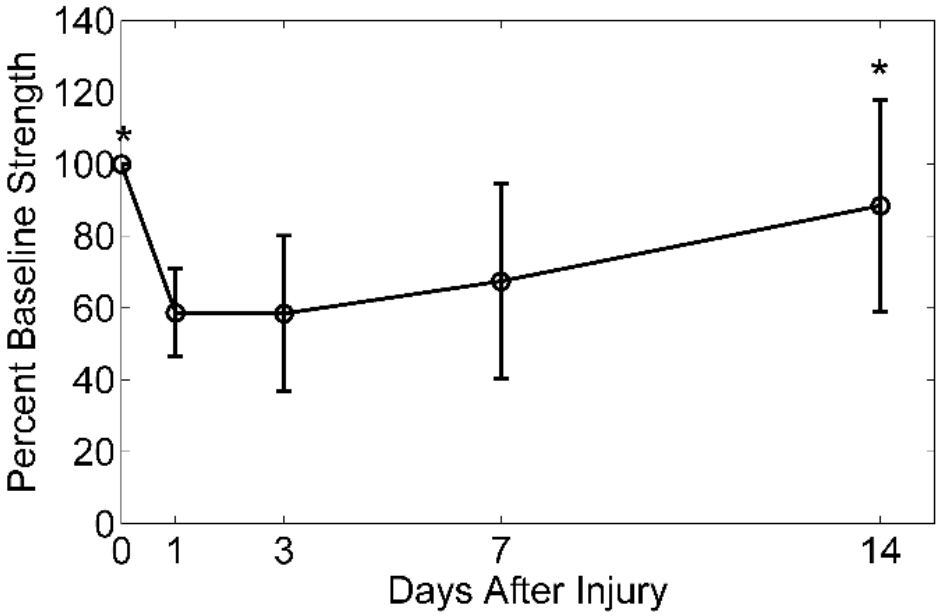

Figure 4.3: The results of the muscle torque-testing are shown for each testing day. The values are all shown as a percentage of the baseline (Day 0) torque values for each rat, and '' indicates significant difference from Day 1 at ($p<0.05$). The muscle strength experienced a significant decrease one day after injury but returned to near-baseline values by Day 14. There were no statistical differences in torque values among Day 1 Day 3, Day 4, and Day 7.*

4.3.2 Ultrasound Images

Injury severity, as determined using the ultrasound image grading scale, followed a similar trend as the muscle strength (Figure 4.4). Signs of muscle damage were seen immediately after injury, with Day 1 showing a mean injury score of 2.03 ± 0.22, which was significantly higher than the pre-injury score of 0.363 ± 0.22 ($p<0.05$). Injury scores for Days 3, 7, and 14 were also significantly higher than Day 0, reflecting the presence of damaged tissue. However, there were no statistical differences between any of the post-contusion injury levels.

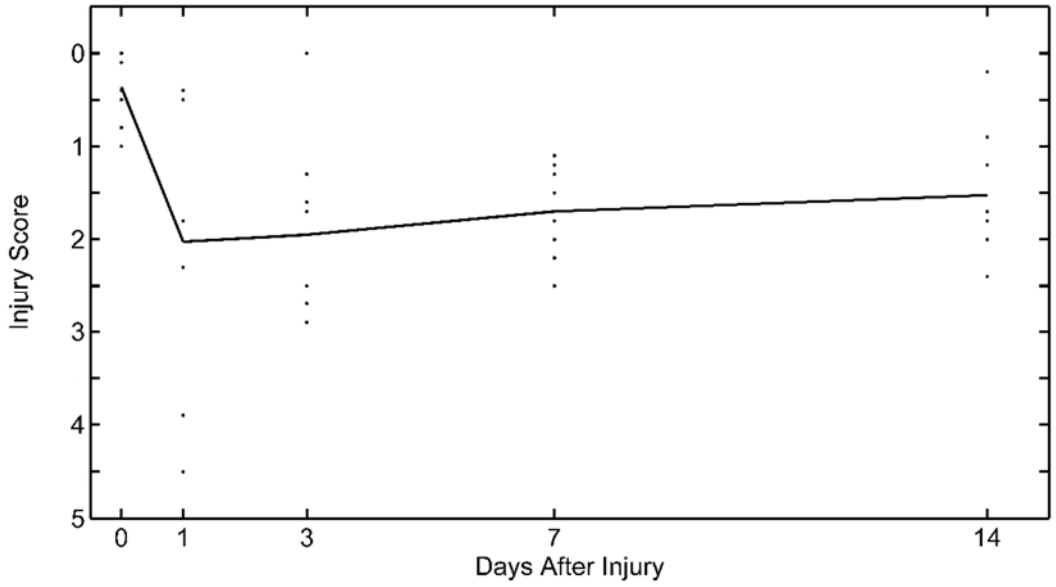

Figure 4.4: Mean ± Std. Dev. Injury Score determined from the ultrasound images at time point. Days 1, 3, 7, and 14 all showed significant increases in Injury Score from Day 0 ($p < 0.05$)*, however no differences were seen between any of the post-injury time points.. The Injury Score follows the same trend as the functional torque data (Figure 4.3).*

Sample B-mode images from Day 0, Day 1, and Day 7 are shown in Figure 4.5. The most severe appearing injuries were seen immediately after injury, with visible swelling and fluid build-up present. However, by Day 7, most of the acute damage was no longer seen in the ultrasound images, with injury primarily being indicated by loss of definition in the deeper structures, as well as blurring of the muscle striations in the upper-half of the image.

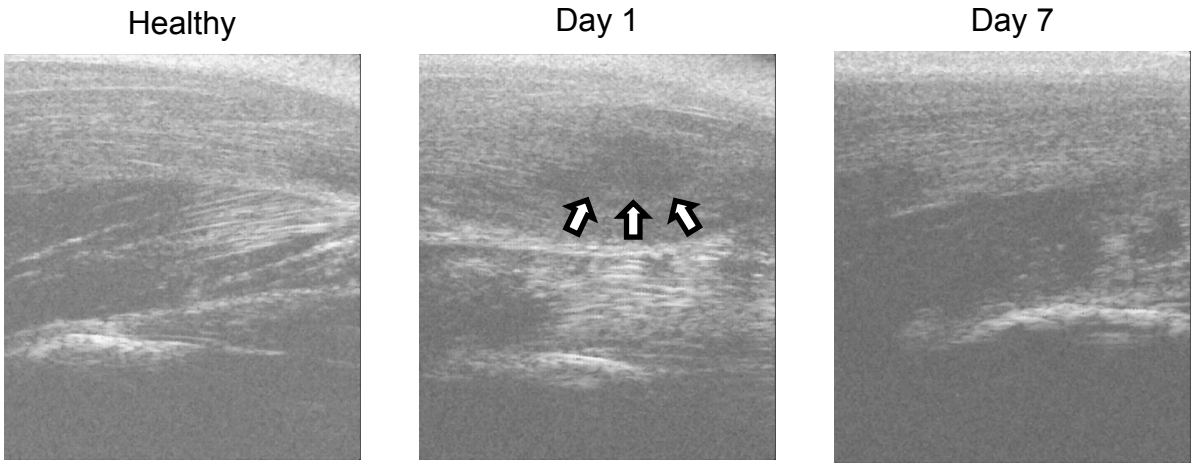

Figure 4.5: Sample ultrasound B-mode images of the rat gastrocnemius before injury, as well as 1 and 7 days after injury are shown. Visible swelling and hematoma (white arrows) were visible by Day 1, but had mostly subsided by Day 7. Although the sonograms show no major evidence of injury by Day 7, the torque-testing results still indicate significant functional impairment.

Injury score was negatively correlated with muscle strength ($N = 40$ and $p < 0.005$), with a regression-line slope $m = -0.188$. This relationship accounts for a relatively small portion of the total data variation, with $R^2 = 0.347$, as seen in Figure 4.6. There were no differences in the mean injury score between any of the rats ($p < 0.05$), but the regression slopes varied greatly between rats, possibly indicating variable degrees of contusion severity.

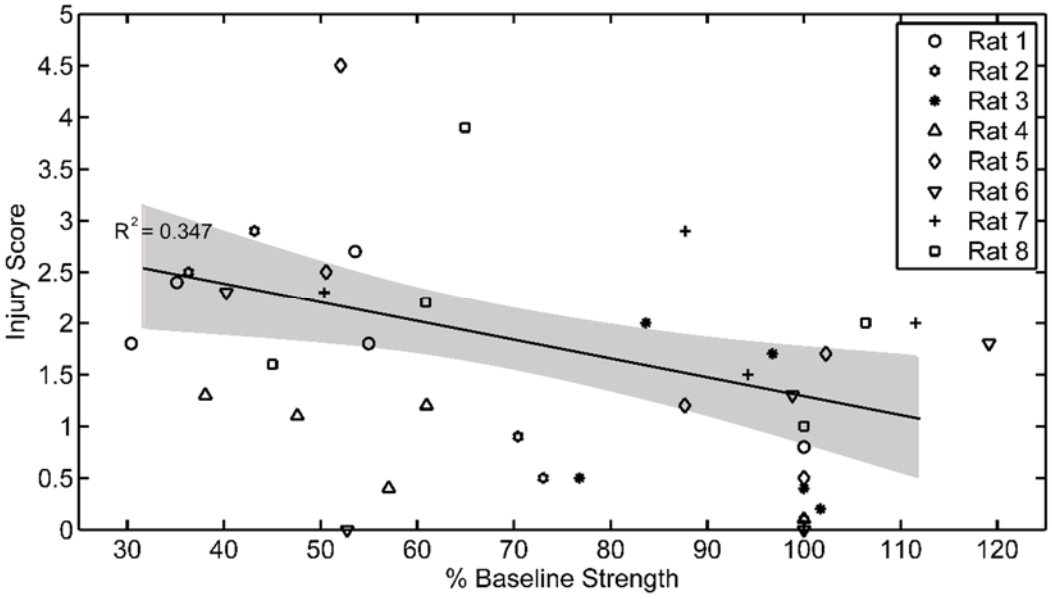

Figure 4.6: Muscle strength (functional torque testing) vs. Injury score for each of the eight rats. Injury score exhibited an overall negative correlation to muscle strength at significance $p < 0.005$. *The shaded gray area indicates the* 95% *confidence interval for the linear fit.*

4.4 Discussion

Quasi-static ultrasound elastography was performed on the right gastrocnemius of 12 Wistar rats before contusion injury and throughout the healing process. *In-situ* torque testing was used to measure muscle health at each imaging time point. Both the functional testing and image analysis showed significant injury and a trend towards recovery over the two-week period. However, the day-to-day variations in muscle strength and B-mode images were not sufficient to show statistically significant incremental changes. Improvements to the imaging system, test protocol, a larger image training set, and additional animals in the study may help improve the accuracy and day-to-day resolution of injury detection.

The results of the torque testing indicate a significant injury after the initial contusion, as well as a general two-week long recovery to near-baseline health levels. The lack of

statistical differences between the consecutive testing days is primarily due to the high inter-rat variation in strength levels, which is evident by the high error-bars in Figure 3. The shape of the strength curve is similar to the expected curve seen for both strain [16] and contusion [14,17] injuries, with similar drops in muscle strength immediately after injury followed by a prolonged recovery.

The injury severity scores follow the same general trend as the muscle torque, suggesting successful detection of injury up to 14 days after injury. However, the lack of day-to-day changes in injury severity does not allow for continuous monitoring of injury progression. The highest individual injury scores were seen on Day 1, with significant swelling and visible hematoma present in the sonograms. Subsequent days showed few incidences of acute trauma, but the images still evidenced signs of muscle inflammation and fiber damage. This progression of damage seen in the ultrasound images closely relates to the four histologic stages seen by Crisco et. al. [17]: acute injury, degeneration, regeneration, and normalization, with the most severe injuries occurring between 0-3 days after injury.

Injury score correlated well to muscle strength, but only accounted for a relatively small portion of the total variation in the data. The large spread seen in Figure 4.6 can most likely be attributed to the wide range of torque values and injury scores at each time point, and may be a result of variability in the initial injury severity. The regression results suggest it may be able to predict estimates of muscle functional health using ultrasound imaging alone. This capability would allow for continuous monitoring of muscle healing after injury without the need for invasive functional testing procedures. However, additional refinement is needed to reduce the high degree of variation in the muscle strength vs. injury score relationship.

Future work will aim to reduce these variations by improving the injury grading system and expanding the image training sets. Additional changes will include increasing the number of trained observers to examine the effects of operator subjectivity on the resulting diagnoses. Incorporating histologic examination of the muscle tissue at each time point will help understand the tissue mechanisms underlying the damage seen in the ultrasound images, and enable a more precise classification of acute injury, degeneration, regeneration, and normalization.

Further improvements to the study can be achieved by increasing the number of rats, as well as refining the ultrasound imaging protocol. An increased number of rats may help identify the day-to-day fluctuations in muscle strength following injury, and enable finer temporal resolution of muscle health. Although the imaging muscle compression and ultrasound imaging windows were fairly consistent throughout the study, improvements to the imaging protocol may involve fixing the transducer placement on the posterior surface of the gastrocnemius and applying the compression to the anterior tibia. By separating the transducer placement and compression we can better stabilize the imaging window and ensure a uniform stress application. Further mechanical stabilization of the compression can be achieved using a standard linear array transducer rather than a single oscillating piezoelectric crystal. The decreased vibration noise will help remove extraneous motion from the scanning procedure.

4.5 Conclusion

Muscle functional testing and ultrasound imaging were used to determine damage severity at known levels of skeletal muscle health after a contusion injury. Ultrasound is shown to be able to detect the tissue damage up to two weeks post-injury, and the

injury grading system exhibited a negative correlation to muscle health. These results indicate that ultrasound imaging may be able to replace functional testing as a means to quantify muscle health after injury. However, further refinement of the imaging procedure is needed before day-to-day differences in muscle health can be detected with ultrasound. Future work will focus on fine-tuning damage grading scale and imaging protocol to reduce the overall variation in the injury scores.

REFERENCES

1. Ekstrand J, Hägglund M, Waldén M. Epidemiology of muscle injuries in professional football (soccer). Am J Sports Med. 2011 Jun;39(6):1226–32.

2. Huard J, Li Y, Fu FH. Muscle injuries and repair: current trends in research. J Bone Joint Surg Am. 2002 May;84-A(5):822–32.

3. Järvinen T, Järvinen M, Kalimo H. Regeneration of injured skeletal muscle after the injury. Muscles, ligaments …. 2013;3(grade II):337–45.

4. Kasemkijwattana C, Menetrey J, Somogyl G, Moreland MS, Fu FH, Buranapanitkit B, et al. Development of approaches to improve the healing following muscle contusion. Cell Transplant. 7(6):585–98.

5. Woodhouse JB, McNally EG. Ultrasound of skeletal muscle injury: an update. Semin Ultrasound CT MR. Elsevier Inc.; 2011 Apr;32(2):91–100.

6. Järvinen T a H, Järvinen TLN, Kääriäinen M, Aärimaa V, Vaittinen S, Kalimo H, et al. Muscle injuries: optimising recovery. Best Pract Res Clin Rheumatol. 2007 Apr;21(2):317–31.

7. Campbell SE, Adler R, Sofka CM. Ultrasound of muscle abnormalities. Ultrasound Q. 2005;21(2):87–94; quiz 150, 153–4.

8. Martinson H, Stokes MJ. Measurement of anterior tibial muscle size using real-time ultrasound imaging. Eur J Appl Physiol. 1991;250–4.

9. Pillen S, van Keimpema M, Nievelstein RA, Verrips A, van Kruijsbergen-Raijmann W, Zwarts MJ. Skeletal muscle ultrasonography: Visual versus quantitative evaluation. Ultrasound Med Biol. 2006;32(9):1315–21.

10. Su E, Koh C, Mcnally EG. Ultrasound of Skeletal Muscle Injury. 2007;

11. Campbell SE, Adler R, Sofka CM. Ultrasound of muscle abnormalities. Ultrasound Q. 2005 Jun;21(2):87–94;153–4.

12. Su E, Koh C, Mcnally EG. Ultrasound of Skeletal Muscle Injury. Ultrasound. 2007;

13. Heckmatt J, Leeman S, Dubowitz V. Ultrasound imaging in the diagnosis of muscle disease. J Pediactrics. 1982;101(5):656–60.

14. Delos D, Leineweber MJ, Chaudhury S, Alzoobaee S, Gao Y, Rodeo S a. The Effect of Immediate and Delayed Injection of Platelet-Rich Plasma (PRP) on Muscle Contusion Healing in the Rat. Orthop J Sport Med. 2013 Sep 20;1(4 Suppl):2013–5.

15. Crisco JJ, Hentel KD, Goehner K, Jokl P, Haven N. Maximal contraciton lessens impact response in a muscle contusion model. Science (80-). 1996;29(10):1291–6.

16. Hammond JW, Hinton RY, Curl LA, Muriel JM, Lovering RM. Use of autologous platelet-rich plasma to treat muscle strain injuries. Am J Sports Med. 2009 Jun;37(6):1135–42.

17. Crisco JJ, Jokl P, Heinen GT, Connell MD, Panjabi MM. A Muscle Contusion Injury Model. Am J Sports Med. 1994;(July).

CHAPTER 5

CONCLUSIONS AND FUTURE WORK

5.1 Conclusions

5.1.1 Summary

Skeletal muscle injuries are frequent in sports and exercise, accounting for between 20-55% of all sports injuries [1–3]. Muscle strains and contusions make up the majority of these injuries, and can range from mild to severe [4,5], with the worst cases often requiring radiologic assistance. Medical imaging of these injuries can provide valuable insight into the nature and extend of tissue damage, and MRI is currently the gold standard for use with muscle injury. However, due to the cost, wait-time, and limited availability of MRI systems, radiologic assistance is not standard practice, and diagnoses are performed based on knowledge of the injury mechanism and exhibited symptoms [3]. Due to its affordability, portability and real-time imaging capabilities, ultrasound imaging is becoming increasingly recognized as a useful tool for soft tissue imaging and a viable alternative to MRI for early-stage diagnosis and injury monitoring [6,7]. Furthermore, the addition of ultrasound elastography (USE) to traditional imaging techniques provides supplementary information about tissue stiffness and structural integrity that might not otherwise be attainable. Since many tissue types may appear similar in ultrasound images, including fibrotic tissue and fatty infiltration, this mechanical information is especially useful in distinguishing between tissue types during muscle regeneration.

The primary goal of this thesis was to develop ultrasound elastography as an affordable, fast, and readily-available alternative to MRI for both early-stage diagnosis of muscle injury and rehabilitation monitoring. Due to the highly operator-dependent nature of ultrasound imaging, and specifically USE, completion of this goal first required consistent, repeatable, reproducible strain images. Therefore, this thesis sought to accomplish three specific aims: (1) increase intra-subject repeatability and reproducibility, (2) test the feasibility of using principal component analysis

(PCA) to account for normal inter-subject and inter-operator variations, and (3) employ USE and principal component analysis to identify damaged tissue and monitor muscle regeneration after contusion injury.

The results of these studies show that a simple averaging procedure can be used to increase strain-image repeatability using as few as eight repeated compression cycles. Furthermore, USE combined with PCA may be feasible as a diagnostic tool for muscle injury, but further work is needed to develop this technique.

5.1.2 Chapter Overview

Chapter 2 introduced averaging as an appropriate technique for improving the repeatability and reproducibility of ultrasound strain images. Rather than using just a single scan selected from several repeated compressions, an average of 4-8 scans exhibited lower noise levels without loss of image features. These conclusions are evidenced by decreased norm error between pairs of averaged images compared to the gold-standard automated systems. Therefore, averaging may be an ideal tool for improving image quality and diagnostic power of quasi-static elastography of muscle tissue, without the need for additional machinery.

The results of Chapter 3 indicate that principal component analysis, combined with the *damage-displacement* metric, may be feasible tools for locating and quantifying damage to skeletal muscle. A finite element model simulating both force-controlled quasi-static ultrasound elastography, was used to determine the effects of imaging window, compression magnitude, and tissue mechanical properties on the resulting strain distributions of skeletal muscle. These images were input into a principal component algorithm to determine the corresponding eigenimages. Strain images from a finite element model of contused skeletal muscle were compared against their closest principal component representations using the *damage-displacement* technique for a range of injury size and severity. These comparisons clearly identify the presence of abnormal tissue for injuries as

small as 2mm and ±5% changes in mechanical properties. A high contrast-to-noise ratio in the resulting *damage-strain* allows precise location of injured areas using visual inspection.

Chapter 4 used ultrasound imaging to detect and monitor skeletal muscle damage in a rat injury model of the gastrocnemius. Functional testing confirmed significant injury was present, which were corroborated by visual signs in injury in the ultrasound images. A custom scoring system was developed to grade damage severity at each time point. These Injury Scores showed significant damage to the muscle after injury, but were not able to identify day-to-day changes in tissue health. Future iterations of this study will incorporate histology to further evaluate the injury mechanisms and confirm the presence of injury and muscle regeneration.

5.2 Clinical Significance

The integration of USE into current diagnostic procedures for skeletal muscle injury can provide valuable information about tissue damage and morphology. This thesis improved upon current USE scanning procedures by increasing strain image repeatability and reproducibility without the need for additional automated compression equipment. These improvements decrease both equipment and training costs the expense of a minimal increase in scanning time. The addition of PCA and *damage-displacement* techniques allow for precise quantification and location of muscle damage without the need for mathematical models of tissue mechanical behavior. Quantification of tissue damage enables clinicians to specifically grade the injury severity and help determine treatment options. Implementation of these techniques into current diagnostic procedures may result in faster diagnosis and a more complete understanding of the injury, which ultimately can be used to prescribe custom treatment options and shorten healing time.

5.3 Future Work

This thesis lays a foundation for establishing USE as a powerful diagnostic tool for skeletal muscle injury. The techniques described in these studies can be refined and improved upon to address

both clinical and research needs.

Improvements to the imaging protocol and injury grading scale can improve transducer stabilization and image quality, and allow for more precise monitoring of injury from ultrasound images, respectively. A larger training set and additional rats for testing may help decrease the variance of both the injury severity and torque measurements, thereby increasing the study power. Additional improvements to Chapter 4 will incorporate histology as a further confirmation of injury and regeneration. Histology allows for more accurate identification of tissue morphology, and can be compared against the strain maps to assist in identifying fibrotic and fatty infiltration of the muscle tissue.

A more complete understanding of the effects of noise on PCA representation of displacement patterns from transverse compression is needed. Specifically, it would be interesting to explore the effects of different loading conditions on the same tissue at different noise levels. Differences in displacement patterns of healthy tissue undergoing different loading types may significantly affect the strength of the individual principal components. Exploring these boundary condition effects can help determine optimum or ineffective loading techniques for clinical application of PCA to ultrasound elastography.

Finally, if the noise effects are understood, future work with PCA and skeletal muscle will use both finite elements and ultrasound elastography to better describe the relationship between injury and its result on the mechanical properties of the tissue. The finite element input parameters can be refined using mechanical testing to better estimate the healthy muscle material parameters. Ultrasound elastography will be used to generate *damage-displacement* maps of injured muscle, thereby allowing for the identification of the characteristic displacement and strain patterns corresponding to specific types and severity of injury. This injury data will be used to perform a parametric analysis of the finite element model, simulating damaged tissue of various shapes and

sizes with a range of mechanical properties. Comparison of the finite element displacement and strain maps to the elastography results will allow for direct correlation of known injury types and severity with the finite element tissue stiffness properties. These studies will focus on contusion and strain injuries, in particular, since they account for the majority of muscle injuries.

REFERENCES

1. Järvinen T, Järvinen M, Kalimo H. Regeneration of injured skeletal muscle after the injury. Muscles, ligaments …. 2013;3(grade II):337–45.

2. Ekstrand J, Hägglund M, Waldén M. Epidemiology of muscle injuries in professional football (soccer). Am J Sports Med. 2011 Jun;39(6):1226–32.

3. Valle X. Clinical practice guide for muscular injuries: epidemiology, diagnosis, treatment and prevention. Br J Sports Med. 2011 Jan 20;45(2):e2–e2.

4. Beiner JM, Jokl P, Cholewicki J, Panjabi MM. The effect of anabolic steroids and corticosteroids on healing of muscle contusion injury. Am J Sports Med. 1999;27(1):2–9.

5. Delos D, Leineweber MJ, Chaudhury S, Alzoobaee S, Gao Y, Rodeo S a. The Effect of Immediate and Delayed Injection of Platelet-Rich Plasma (PRP) on Muscle Contusion Healing in the Rat. Orthop J Sport Med. 2013 Sep 20;1(4 Suppl):2013–5.

6. Campbell SE, Adler R, Sofka CM. Ultrasound of muscle abnormalities. Ultrasound Q. 2005;21(2):87–94; quiz 150, 153–4.

7. Martinson H, Stokes MJ. Measurement of anterior tibial muscle size using real-time ultrasound imaging. Eur J Appl Physiol. 1991;250–4.

APPENDIX A

THE EFFECT OF PLATELET-RICH PLASMA (PRP) ON MUSCLE CONTUSION HEALING IN A RAT MODEL[2]

A.1 Introduction

Muscle contusions caused by blunt, nonperforating trauma are amongst the most common injuries in athletes[10]. Pain and restricted range-of-motion due to these injuries can lead to decreased performance and limited ability to play. Conservative management, including rest, ice, compression, elevation (RICE) is often considered the treatment of choice. However, symptoms may persist for an extended period of time and more effective treatments are needed.

Platelet-rich plasma (PRP) is a locally administered agent that is being investigated for use in soft tissue healing. PRP is a concentrated solution of platelets derived from whole blood. Though the specific elements of PRP have yet to be completely defined, a concentration of approximately one million platelets or more per microliter has been shown to be clinically useful.[13] Activation of the platelets, whether *ex vivo* (by thrombin and calcium) or *in vivo* by exposure to collagen[7] leads to local release of growth factors from the alpha and dense granules located in the platelet. Growth factors found within α-granules include platelet-derived growth factor (PDGF), vascular endothelial growth factor (VEGF), transforming growth factor beta-1 (TGF-β_1), epidermal growth factor (EGF), basic fibroblast growth factor (bFGF), and insulin-like growth factor-1 (IGF-1).[2]These growth factors are associated with the initiation of a healing cascade leading to cellular chemotaxis, angiogenesis, collagen matrix synthesis and proliferation. Adenosine, serotonin, histamine and calcium are found in the dense granules.

[2] Delos, D. Leineweber, MJ. Chaudhury, S. Alzoobaee, S. Gao, Y. Rodeo, S. "The Effect of Platelet-Rich Plasma (PRP) on Muscle Contusion Healing in a Rat Model", *American Journal of Sports Medicine*, April 2014.

The clinical literature is limited with regards to PRP and soft tissue healing, though initial small case series showed promising results. In a case-control study, Sanchez et al reported that six athletes that underwent open Achilles tendon repair along with injection of PRP recovered range-of-motion sooner and were able to return to running and training quicker than six athletes who underwent open Achilles repair without PRP injection.[21] Mishra et al reported significant pain relief in patients who received a single PRP injection for chronic elbow epicondylar pain at final follow-up.[16] More recently, a randomized trial comparing PRP to corticosteroid injection for recalcitrant lateral epicondylitis showed superior outcomes in the PRP group.[17]

There are very little data on the effect of PRP on muscle injury. A recent study utilizing a rat model found a positive effect of PRP after repeated muscle strain injuries.[9] However, currently, there are no published clinical or animal studies investigating the effects of PRP on healing of skeletal muscle contusion, in this study we employed a drop-mass technique in rats to create a controlled muscle contusion injury and then evaluated the effects of local PRP administration on muscle healing. We hypothesized that local injection of PRP would lead to accelerated healing rates compared to controls. We also hypothesized that delayed administration of PRP would lead to a blunted response compared to immediate treatment.

A.2 Materials and Methods

This study was approved by the Hospital for Special Surgery Institutional Animal Care and Use Committee (IACUC). Forty-six (46) male Lewis rats each underwent a single blunt, non-penetrating impact to the gastrocnemius muscle via a drop-mass technique. The rats were separated into 4 groups, with each rat undergoing injection into the injured gastrocnemius muscle in the following manner:

- Rats in Group 1 (n=11) underwent a single injection of 100ul of saline within 2 hours of injury (CTRL-Controls)
- Rats in Group 2 (n=12) underwent a single injection of 100ul of rat PRP within 2 hours of injury (PRP 0)

- Rats in Group 3 (n=12) underwent a single injection of 100ul rat PRP on post-injury day #1 (PRP 1)
- Rats in Group 4 (n=11) underwent a single injection of 100ul of rat PRP on post-injury day #3 (PRP 3)

After the injury, rats were allowed unlimited activity. The primary outcome measurement was maximal isometric torque strength of the injured muscle, which was performed prior to injury as well as on post-injury days 1, 4, 7, 10, and 14. All animals were sacrificed on post-injury day 15.

A.2.1 Muscle Contusion Injury Model

The technique was adapted from that described by Crisco et al.[5] Briefly, the rats were anesthetized and placed in the prone position with the right hindlimb secured to a platform. The ankle was placed in the neutral position with the knee extended. Electrodes were placed subcutaneously on either side of the gastrocnemius muscle of the experimental leg. The muscle was then stimulated to tetanus for a period of 1 second throughout impaction to provide the most reliable/reproducible injury.[4] A mass weighing 500g was dropped from a height of 33 cm onto an impactor shaped as a sphere on its bottom that directly contacted the skin over the rat gastrocnemius muscle, causing the injury (Figure A.1). A pilot study demonstrated that this protocol results in a clinically

relevant, reproducible injury (results unpublished).

Figure A.1: Photographic image of injury model setup with rat lying prone and impactor striking gastrocnemius of hindlimb.

A.2.2 PRP Production

Seventeen (17) male Lewis rats were used for the purposes of PRP production. Our laboratory developed a custom protocol for preparing rat PRP as follows. Whole blood was drawn from Lewis rats via intracardiac puncture following euthanasia by CO^2 inhalation. The blood was pooled and collected into blood tubes containing the anticoagulant citrate phosphate dextrose (CPD). It was then centrifuged at 1000 g for 30 minutes at 4ºC. This setting was determined to produce platelet concentrations of at least 4 times whole blood levels, following a pilot experiment evaluating different centrifugation times and speeds (results unpublished). The platelet rich fraction of the supernatant was then isolated.

All injections were performed within 2 hours of PRP preparation. In brief, 100ul of PRP solution was drawn into a 1cc tuberculin syringe with a 27-gauge needle. The volume of injection was the same as that previously used in another study utilizing a rat muscle injury model.[9] The injection site was prepped in sterile fashion and the needle was inserted through the skin into the medial head of the gastrocnemius in the region of injury. Approximately half of the volume was injected

into the medial gastrocnemius. Then without completely withdrawing the needle out of the skin, it was redirected into the lateral head to allow for injection of the remaining volume. No additive was used to activate the PRP prior to injection as previous work has shown that PRP can be activated by exposure to collagen alone.[7]

A.2.3 Platelet concentration and growth factor analysis

The concentration of platelets in the PRP was determined using an automated cell counter. Aliquots from each preparation were analyzed for platelet cell count to ensure the concentration was at least four times whole blood levels.

The concentrations of PDGF, VEGF, and TGF-β were determined by ELISA immunoassays (Quantikine Immunoassay kits, R&D systems, Minneapolis, MN) performed by Harvest Technologies (Plymouth, MA) on an aliquot of prepared PRP.

A.2.4 Biomechanical Testing (Maximal Isometric Torque Testing)

The primary outcome tested was maximal isometric torque strength of the gastrocnemius complex as a percentage of baseline (pre-injury) values. For torque testing, the animal was first sedated with inhalation anesthesia and placed supine onto a custom platform. The foot was secured onto a footplate and the tibia was stabilized with a Kirschner wire placed through the proximal metaphysis (Figure A.2). A C-clamp was used to secure the thigh to a post with the knee at 90^{o} of flexion.

Muscle stimulation was performed using monopolar needle electrodes placed subcutaneously in the popliteal fossa/proximal calf. Contraction was induced by stimulation with a 15 mA constant current and voltage was optimized for maximum contraction. All isometric contractions were performed with the foot orthogonal to the tibia (considered 0°). Maximal isometric torque testing was performed on the injured limb prior to injury (baseline value), 5 minutes after injury, and then

1, 4, 7, 10, and 14 days after injury.

Figure A.2: Photographic image of rat being prepared for torque testing. The foot is placed on a footholder attached to a torque sensor and the tibia is secured with a wire. Stimulation is performed with subcutaneous electrodes (not shown).

A.2.5 Histologic Analysis

Upon sacrifice, six rats from each group were chosen at random for tissue harvest and histologic processing. Briefly, the injured gastrocnemius muscle was carefully dissected and placed in formalin for 72 hours. The tissue was then embedded in paraffin and sectioned in the axial plane in 5um thickness slices.

A.2.6 Evaluation of muscle regeneration

Tissue specimens were stained with hematoxylin and eosin (H and E) to evaluate the general morphology and to determine the number of centronucleated muscle fibers. Centronucleated fibers are a marker of muscle regeneration.[12] Analysis of regenerating myofibers was performed by counting the number of fibers in 10 randomly selected microscope fields per sample at 100 times magnification using a light microscope (Nikon Optiphot; Nikon Corporation, Japan) and obtaining pictures with a digital camera (Nikon DMX1200; Nikon Corporation, Japan)

A.2.7 Evaluation of fibrosis

Masson's trichrome staining (IMEB Inc, Chicago, Illinois) was used to evaluate the extent of fibrosis in the area of injury. After Masson trichrome staining, specimens were viewed at 40 times magnification using a light microscope and photomicrographs were obtained with a digital camera. The ratio of the fibrotic area to the total cross-sectional area was calculated to estimate fibrosis formation using NIH Image J software (NIH, Bethesda).

A.2.8 Immunohistochemical analysis

Serial sections were treated with 3% H_2O_2 to quench endogenous peroxidase activity, and nonspecific antibody binding was blocked with serum-free protein block. Each primary antibody was applied to separate serial sections for 60 min at room temperature. Bound antibodies were visualized using biotinylated link antibody and streptavidin-HRP system developed with 3,3' diaminobenzidine (D.A.B., Dako Corp., Carpinteria, CA) as a substrate chromogen. We used the following antibodies to localize hematopoietic lineage cells: mouse anti-rat ED1-macrophage (ED1 antigen is a lysosomal glycoprotein expressed only by a subpopulation of macrophages and monocytes) and mouse anti-rat ED2-macrophage (ED2 antigen is a membrane glycoprotein found only on mature tissue macrophages) (Serotec Inc., Raleigh, NC). The sections were counterstained with Mayer's hematoxylin. Semi-quantitative analysis was performed by reviewing 10 randomly selected fields per sample at 100 times magnification using a light microscope and obtaining pictures with a digital camera. A grading system was used as follows: Grade 0 (no positively staining cells), Grade 1 (scant number of positively staining cells in the entire field), Grade 2 (moderate number of positively staining cells in the entire field), Grade 3 (large number of positively staining cells in the entire field).

A.2.9 Statistical Analysis

A power analysis using pilot data was performed using the assistance of the institutional

biostatistics department prior to commencing the study. This analysis determined that with alpha set at 0.05 (α=0.05) and beta set at 0.20 (β=0.20), 12 animals per group would be required.

Contractile, histological, and immunohistochemical data from each experiment were analyzed with single-factor analysis of variance (ANOVA) using SigmaStat software (Systat Software Inc, Chicago, Ill, USA).

A.3 Results

Twelve rats underwent the procedure in the immediate treatment and PRP Day#1 groups. Eleven rats underwent the procedure in the control and PRP day# 3 groups, due to anesthetic complications resulting in accidental death at the time of surgery. Mean rat weight was 319 (±15) grams with no significant difference between the groups (p=0.249).

A.3.1 Platelet and growth factor concentrations

The mean platelet concentration in the PRP was $2.19x10^6$ ($\pm 2.69x10^5$) per uL. This was over 4 times greater than mean whole-blood platelet levels in a randomly selected sample of whole blood obtained prior to centrifugation. The mean white blood cell count in the PRP was $22.54x10^3$/uL. Mean white blood cell count in the rat whole blood was $5.21x10^3$/uL.

In the aliquot of PRP tested for specific growth factors, PDGF-AB, VEGF and TGF-β concentrations were 330pg/ml, 18pg/ml, and 85ng/ml, respectively. PDGF-AB, VEGF and TGF-β concentrations were 125pg/ml, 10pg/ml, and 32ng/ml, respectively, in whole blood. Thus, PDGF-AB levels were 2.6 times greater in the PRP compared to whole blood levels from the same sample; VEGF levels were 1.8 times greater, and TGF-β levels were 2.7 times greater, respectively.

A.3.2 Isometric Torque Testing

Each group demonstrated statistically significant decreases ($p<0.05$) in maximal isometric torque

strength after injury compared to pre-injury levels, with the lowest values observed by approximately day 4-7. (see Tables 2a-d; Figure A.3) This was followed by significant increases ($p<0.05$) back towards baseline values by post-injury day 14. There were no statistically significant differences between the control and treatment groups at any of the time-points.

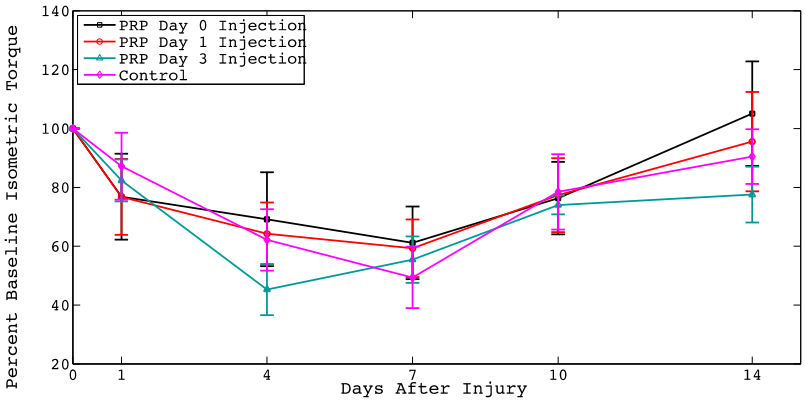

Figure A.3: Graphical representation of mean maximal isometric torque strength by group over time.

A.3.3 Histologic Analysis (performed on samples retrieved after sacrifice, post-injury day #15)

Histologic analysis was performed on samples retrieved after sacrifice, post-injury day #15. The control group demonstrated the highest mean percentage of centronucleated fibers per visual field (3.31%±5.10%) and the PRP Day 0 group demonstrated the lowest (0.62%±1.59%). The PRP Day 1 group had a mean percentage of 3.24%±5.77% and the PRP Day 3 group had a mean

percentage of 2.13%±3.26%. However, the difference in the percentage of centronucleated

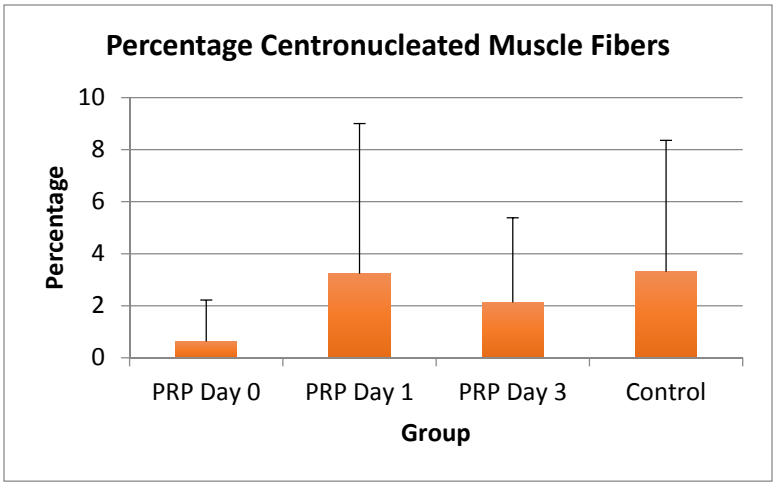

muscle fibers between treatment and control groups was not statistically significant (Figure A.4).

Figure A.4: Graph depicting the percentage of centronucleated muscle fibers per group.

The animals treated with PRP on post-injury day #1 demonstrated the highest volume percentage of fibrotic (scar) tissue (3.11%±3.65%) and the control group demonstrated the lowest (0.89%±1.95%). The PRP Day 0 and the PRP Day 3 groups had a mean volume percentage of 1.37%±2.44% and 2.78%±4.75%, respectively. However, the difference in the percentage of fibrotic (scar) tissue between groups was not statistically different between any of the groups.

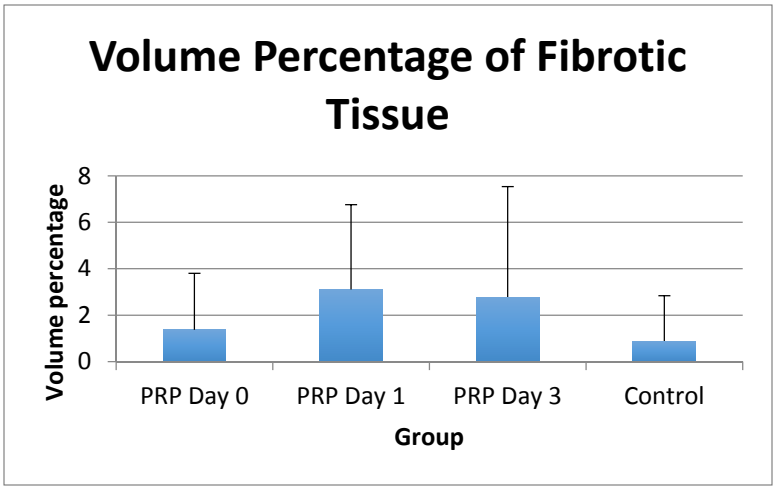

(Figure A.5)

Figure 5: Graph depicting the percentage of volume of fibrotic tissue per group.

A.3.4 Immunohistochemical Analysis

The group treated with PRP immediately after injury demonstrated the lowest mean immunohistochemical grade (0.22±0.41) whereas the group that received PRP on post-injury day #3 had the highest mean immunohistochemical grade (0.42±0.61). The group treated with PRP on day #1 and the control group had a mean grade of 0.26±0.74 and 0.34±0.58, respectively. There were no statistically significant differences in mean immunohistochemical grade between any of the groups. (p=0.1158) (Figure A.6).

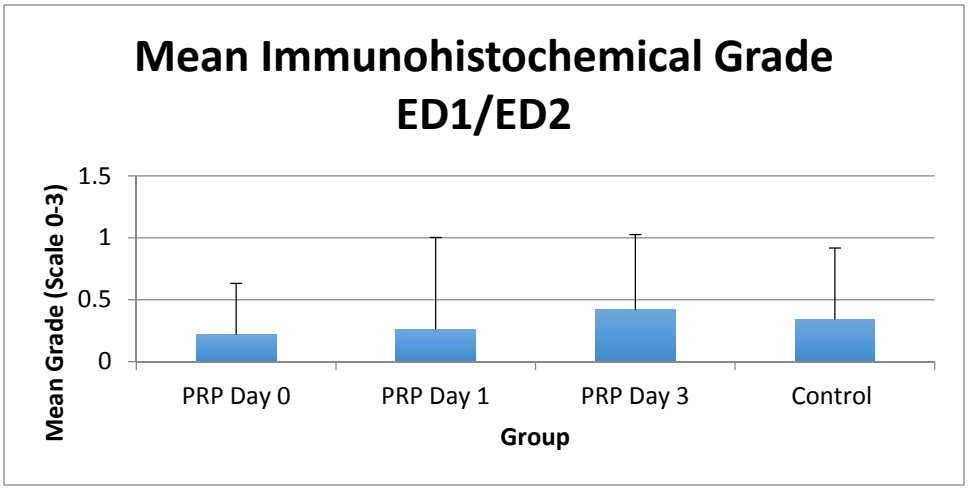

Figure A.6: Graph depicting the mean immunohistochemical grade per group (antibody testing for ED1/ED2).

A.4 Discussion

Platelet rich plasma (PRP) has received a tremendous amount of attention both in the medical literature as well as the lay press over the last several years. Initial reports demonstrated positive findings, but these studies were limited primarily to small retrospective case series.[15,16,21] More recently, clinical studies of higher-level quality[6,8,17,19] have been published but these have shown variable results. A recent randomized, controlled trial demonstrated no effect on Achilles tendonitis treated with PRP injection and eccentric exercise compared to controls[6]; however, a

randomized, controlled trial showed that PRP treatment of lateral epicondylitis had superior outcomes compared to steroid injections.[17] Some criticisms associated with these studies include the lack of isolated treatment and the use of a treatment (steroid injection) that is not universally regarded as the gold standard. In addition, other studies, including one from our institution. have shown no benefit in the treatment of rotator cuff injuries with platelet-rich therapies.[3,19,23]

PRP has also been used empirically for the treatment of muscle injuries though the literature on the effects of PRP on muscle healing is scant. Sanchez[20] presented a small retrospective series which reported positive findings but was limited in terms of the outcomes tested and the rigor of the study design. The authors reported performing ultrasound-guided injections of PRP into 22 injured muscles in 20 professional athletes. They noted full functional recovery in all patients in half the expected recovery time, without evidence of fibrosis and no-reinjuries upon resumption of normal activities. This study however, is limited to an abstract published at the 2nd World Congress on Regenerative Medicine with no further follow-up. No other level IV or higher clinical study exists regarding PRP and muscle healing.

In the basic science literature, Hammond et al[9] used a rat tibialis anterior strain model and found that PRP provided a positive benefit in terms of faster recovery for those rats that underwent multiple strain injuries but not in those in the single strain protocol group. The authors speculated that since recovery from the high-repetition protocol primarily relies on myogenesis, rather than sarcolemmal repair[12], PRP may be more effective for injuries that rely on muscle regeneration rather than repair. A recently presented abstract by Terada et al[22] also reported positive findings in mice treated with PRP injection and administration of losartan after muscle contusion injury. More specifically, the authors reported improvement in muscle strength after PRP and losartan treatment, as well as enhanced muscle regeneration and angiogenesis with decreased muscle fibrosis.[22]

Our study showed no differences in terms of muscle contractile testing and histologic outcomes with no evidence of increased inflammation by the time of sacrifice. The fact that our study showed no positive effect on healing after treatment with PRP may be due to a number of reasons. We utilized a rat model of muscle injury limited to a single contusion event – as suggested by Hammond et al[9], PRP may be of greater utility in multiple injury scenarios since these injuries may rely primarily on a muscle regeneration mechanism rather than sarcolemmal/muscle repair. Though it was originally thought that recovery of function after skeletal muscle injury is predominately associated with activation and proliferation of myogenic cells (i.e. satellite cells)[1,11,18], recent work by Lovering et al,[12] has shown that there are indeed different mechanisms of recovery after repeat muscle injury compared to single injury. In their rat model, the authors[12] found that inhibition of myogenesis by irradiation prior to injury prevented recovery of contractile function after multiple strain injuries but not after a single strain event. Additionally, with the use of Evans blue dye staining, the authors were able to demonstrate that single repetition muscle strain injuries result predominately in sarcolemmal (membrane) injury followed by early sarcolemmal repair (membrane resealing) rather than satellite cell activation and proliferation. Thus, the absence of a significant difference in the number of regenerative cells between the experimental and control groups may be due more to a limitation in study design. Consideration of these mechanisms of muscle recovery suggests that multiple/repeat contusion injuries may result in muscle recovery patterns reliant more on regeneration (i.e. muscle satellite cell activation and proliferation) rather than repair (membrane healing), which may be a direction for further study.

Additionally, our PRP was prepared according to a protocol we developed and did not rely on a commercial system. However, as our analysis demonstrated, platelet concentration was increased to over four times the baseline whole blood value and specific growth factor concentrations were similarly increased several fold beyond whole blood values. We also chose to utilize the PRP immediately after preparation rather than storing it for later use in order to minimize any effects of prolonged storage or freeze/thaw cycles, as well as the fact that this is how it is typically

prepared and applied clinically.

Our study has the following limitations: (1)The study may have been underpowered to detect small differences between groups; as mentioned in the section above, two groups had animal numbers that were one less than the intended number. This was due to anesthetic complications that occurred at the time of surgery. Nevertheless, based on the post-hoc statistical analyses we do not believe that the addition of one animal in each of those two groups would have made a large difference in the outcomes. (2) The optimal concentration of platelets, timing of injection, and volume of solution to be injected has yet to be determined, especially in animal models. Additional research is needed in order to better define the effects of these variables. (3) The PRP we generated had a relatively high concentration of white blood cells. Though the exact role of leukocytes in PRP is unclear, there is some evidence that increased levels can lead to elevated inflammatory cytokine production[14] and therefore, perhaps, a more catabolic rather than anabolic effect. (4) Only a single dose of PRP was used (i.e. no repeated PRP injections) and (5) The potential benefits of PRP for acute muscle healing may be limited – it may be that chronic injuries/lesions respond better than acute ones.

A.5 Conclusion

In summary, PRP is being used clinically to treat numerous soft tissue injuries (including muscle contusions), though clinical data is limited. In this rat contusion model, *local injection of PRP* into the injured gastrocnemius muscle resulted in *no significant differences in functional outcome at various post-injury time-points*, indicating no likely benefit to healing. Additionally, there was *no significant difference between immediate or delayed administration of PRP.*

Further translational and clinical investigation needs to be performed before PRP can be recommended for the treatment of muscle contusion injuries.

REFERENCES

1. Aärimaa V, Rantanen J, Best T, Schultz E, Corr D, Kalimo H. Mild eccentric stretch injury in skeletal muscle causes transient effects on tensile load and cell proliferation. Scand J Med Sci Sports. 2004;14(6):367–372.

2. Anitua E, Andia I, Ardanza B, Nurden P, Nurden AT. Autologous platelets as a source of proteins for healing and tissue regeneration. Thromb. Haemost. 2004;91(1):4–15.

3. Castricini R, Longo UG, De Benedetto M, et al. Platelet-rich plasma augmentation for arthroscopic rotator cuff repair: a randomized controlled trial. Am J Sports Med. 2011;39(2):258–265.

4. Crisco JJ, Hentel KD, Jackson WO, Goehner K, Jokl P. Maximal contraction lessens impact response in a muscle contusion model. J Biomech. 1996;29(10):1291–1296.

5. Crisco JJ, Jokl P, Heinen GT, Connell MD, Panjabi MM. A muscle contusion injury model. Biomechanics, physiology, and histology. Am J Sports Med. 1994;22(5):702–710.

6. de Vos RJ, Weir A, van Schie HTM, et al. Platelet-rich plasma injection for chronic Achilles tendinopathy: a randomized controlled trial. JAMA. 2010;303(2):144–149.

7. Fufa D, Shealy B, Jacobson M, Kevy S, Murray MM. Activation of platelet-rich plasma using soluble type I collagen. J Oral Maxillofac Surg. 2008;66(4):684–690.

8. Gosens T, Peerbooms JC, van Laar W, Oudsten den BL. Ongoing positive effect of platelet-rich plasma versus corticosteroid injection in lateral epicondylitis: a double-blind randomized controlled trial with 2-year follow-up. Am J Sports Med. 2011;39(6):1200–1208.

9. Hammond JW, Hinton RY, Curl LA, Muriel JM, Lovering RM. Use of autologous platelet-rich plasma to treat muscle strain injuries. Am J Sports Med. 2009;37(6):1135–1142.

10. Holbrook TL, Grazier K, Kelsey JL, Stauffer RN. "The frequency of occurrence, impact, and cost of selected musculoskeletal conditions in the United States.." American Academy of Orthopaedic Surgeons. 1984.

11. Lefaucheur JP, Sébille A. The cellular events of injured muscle regeneration depend on the nature of the injury. Neuromuscul. Disord. 1995;5(6):501–509.

12. Lovering RM, Roche JA, Bloch RJ, De Deyne PG. Recovery of function in skeletal muscle following 2 different contraction-induced injuries. Arch Phys Med Rehabil. 2007;88(5):617–625.

13. Marx RE. Platelet-rich plasma (PRP): what is PRP and what is not PRP? Implant Dent. 2001;10(4):225–228.

14. McCarrel TM, Minas T, Fortier LA. Optimization of leukocyte concentration in platelet-rich plasma for the treatment of tendinopathy. The Journal of Bone and Joint Surgery. 2012;94(19):e143(1–8).

15. Mishra A, Collado H, Fredericson M. Platelet-rich plasma compared with corticosteroid injection for chronic lateral elbow tendinosis. PM R. 2009;1(4):366–370.

16. Mishra A, Pavelko T. Treatment of chronic elbow tendinosis with buffered platelet-rich plasma. Am J Sports Med. 2006;34(11):1774–1778.

17. Peerbooms JC, Sluimer J, Bruijn DJ, Gosens T. Positive effect of an autologous platelet concentrate in lateral epicondylitis in a double-blind randomized controlled trial: platelet-rich plasma versus corticosteroid injection with a 1-year follow-up. Am J Sports Med.

2010;38(2):255–262.

18. Rathbone CR, Wenke JC, Warren GL, Armstrong RB. Importance of satellite cells in the strength recovery after eccentric contraction-induced muscle injury. Am J Physiol Regul Integr Comp Physiol. 2003;285(6):R1490–5.

19. Rodeo SA, Delos D, Williams RJ, Adler RS, Pearle A, Warren RF. The effect of platelet-rich fibrin matrix on rotator cuff tendon healing: a prospective, randomized clinical study. Am J Sports Med. 2012;40(6):1234–1241.

20. Sanchez M, Anitua E. Application of autologous growth factors on skeletal muscle healing. 2nd World Congress on …. 2005.

21. Sánchez M, Anitua E, Azofra J, Andia I, Padilla S, Mujika I. Comparison of surgically repaired Achilles tendon tears using platelet-rich fibrin matrices. American Journal of Sports Medicine. 2007;35(2):245–251.

22. Terada S, Ota S, Kobayashi T, et al., eds. Combination treatment using platelet-rich plasma and an angiotensin II receptor blocker for muscle contusions.

23. Weber SC, Kauffman JI, Parise C, Weber SJ, Katz SD. Platelet-rich fibrin matrix in the management of arthroscopic repair of the rotator cuff: a prospective, randomized, double-blinded study. Am J Sports Med. 2013;41(2):263–270.